Vibrational Relaxation by Methylated Xanthines in Solution: Insights from 2D-IR Spectroscopy and Calculations

Alex T. Hanes, Christopher Grieco,[†] Remy F. Lalisse, Christopher M. Hadad, and Bern Kohler[*]

Department of Chemistry and Biochemistry, The Ohio State University, 100 West 18th Avenue,
Columbus, OH 43210, United States

[†]Permanent address: Department of Chemistry and Biochemistry, Auburn University, Auburn, Alabama 36849, USA

[*]Corresponding author: kohler@chemistry.ohio-state.edu

ABSTRACT

Two-dimensional infrared (2D-IR) spectroscopy, infrared pump-infrared probe (IR-PP) spectroscopy and density functional theory calculations were used to study vibrational relaxation by ring and carbonyl stretching modes in a series of methylated xanthine derivatives in acetonitrile and deuterium oxide (heavy water). Isotropic signals from the excited symmetric and asymmetric carbonyl stretch modes decay biexponentially in both solvents. Coherent energy transfer between the symmetric and asymmetric carbonyl stretching modes gives rise to a quantum beat in the time-dependent anisotropy signals. The damping time of the coherent oscillation agrees with the fast decay component of the carbonyl bleach recovery signals, indicating that this time constant reflects IVR to other solute modes. Despite their similar frequencies, the excited ring modes decay monoexponentially with a time constant that matches the slow decay component of the carbonyl modes. The slow decay times, which are faster in heavy water than in acetonitrile, approximately match ones observed in previous UV pump-IR probe measurements on the same compounds. The slow component is assigned to intermolecular energy transfer to solvent bath modes from low-frequency solute modes, which are populated by IVR and are anharmonically coupled to the carbonyl and ring stretch modes. 2D-IR measurements indicate that the carbonyl stretching modes are weakly coupled to the delocalized ring modes, resulting in slow exchange that cannot explain the common solvent dependence. IVR is suggested to occur at different rates for the carbonyl vs. ring modes due to differences in mode-specific couplings and not to differences in the density of accessible states.

I. INTRODUCTION

The photophysics of DNA nucleobases as monomers and as interacting units in DNA strands has been widely explored in recent decades.[1–10] Ultrafast internal conversion (UIC) deposits more than 4 eV of energy in an unknown number of ground state vibrational modes, which must be dissipated via intramolecular vibrational redistribution (IVR) and intermolecular energy transfer (IET, also called external vibrational relaxation, EVR[11]). Collectively, these vibrational energy relaxation (VER) processes, which cause the photoexcited nucleobase to return to thermal equilibrium with nearby solvent molecules, are often summarized by the term vibrational cooling (VC).[12,13] In aqueous solution, VC is complete in a few ps and the photoprotection afforded by UIC and rapid VC may have contributed to the natural selection of the canonical DNA and RNA nucleobases.[7] Despite a growing understanding of how accessible conical intersections on the excited state potential energy surface give rise to UIC, the interplay between IVR and IET in VC remains uncertain, particularly in aqueous solution where hydrogen bonding can accelerate IET rates and efficiencies.[4,5]

To investigate the role that the solvent plays in VC, researchers often compare the VC dynamics of similarly sized molecules or chemical derivatives, which contain various numbers of hydrogen-bond donors and acceptors that can be used to tune solute-solvent interactions.[14–19] This approach neglects the effects that substituents chosen to alter the number and types of hydrogen bonds may have on intramolecular vibrational degrees of freedom. Even seemingly benign modifications such as isotopic substitution or methylation can alter the vibrational energy landscape that governs the return to thermal equilibrium.[20–22] In fact, some authors have exploited the sensitivity of anharmonic couplings to such modifications in order to control vibrational energy transfer.[23–26] Recently, Schmitz et al.[21] showed that inserting a methylene group between the azide group and the benzene ring of *p*-azidobenzonitrile drastically increases the vibrational energy transfer lifetime from the nitrile to the cyano group from 1.9 ps to 23 ps, illustrating the effect that chemical modifications can have on the anharmonic potential energy surface. It is thus important to carefully consider how intramolecular vibrational coupling affects solvent-dependent VC.

To study VC following UIC, many authors have used transient absorption measurements with electronic pumping and electronic or mid-infrared probing.[4–6,12] It has been suggested that high frequency solute modes are important for vibrational relaxation by highly vibrationally excited nucleobases,[27] counter to the conventional wisdom that vibrational energy transfer from a hot solute molecule to surrounding solvent molecules proceeds overwhelmingly via low-frequency solute vibrations.[4] Middleton et al. proposed that VC of 9-methyladenine proceeds via high frequency solvent modes (>700 cm^{-1}) based on the solvent-isotope effect seen in H_2O and D_2O.[5] It was later shown that VC by xanthine derivatives in CH_3CN and D_2O is sensitive to the number of hydrogen-bond donors.[4] This observation was rationalized by N-D bending modes of the xanthine derivatives that resonantly transfer excess vibrational quanta to hydrogen-bonded solvent molecules in D_2O, a pathway that is not available in CH_3CN.

Because UIC occurs concurrently with VC, the short-time dynamics of the generally slower VC events may be obscured. Additionally, these measurements average over all relaxation rates of the subset of modes of the hot ground state molecules that are strongly coupled to electronic absorption, making it difficult to discern mode-specific vibrational relaxation. On the other hand, infrared pump-infrared-probe (IR-PP) and two-dimensional infrared (2D-IR) spectroscopy can monitor vibrational dynamics in the ground electronic state, revealing details about relaxation of additional modes. IR-PP spectroscopy is commonly used to monitor vibrational population lifetimes, while 2D-IR spectroscopy can characterize the anharmonic vibrational potential without the need for isotope labeling.[28,29] 2D-IR spectroscopy has the added benefit of resolving relaxation or energy transfer pathways induced by the pump, allowing one to monitor pathways that are difficult to observe by one-dimensional spectroscopies. Together, IR-PP and

2D-IR spectroscopy make it possible to study VER processes in much greater detail and without interference from simultaneous electronic relaxation.

Here, IR-PP and 2D-IR measurements are used to study VER in the electronic ground state by modes of various methyl-substituted xanthine derivatives in the double-bond stretching region (*ca.* 1500-1750 cm^{-1}). The character of the IR active modes in the double-bond stretching region was determined from normal mode calculations. 2D-IR spectroscopy was used to determine the anharmonic coupling between these modes, including the strong coupling between the symmetric and asymmetric carbonyl stretching modes. Despite similar anharmonic couplings and mode character of the double-bond stretching modes, IR-PP studies reveal significant differences in the vibrational relaxation of the carbonyl vs. ring stretching modes.

II. RESULTS

The molecular structures of caffeine (1,3,7-trimethylxanthine), paraxanthine (1,7-dimethylxanthine), and theophylline (1,3-dimethylxanthine) are shown in **Fig. 1** together with that of the xanthine parent compound, which is included to show the atom numbering used for all compounds. The structures in **Fig. 1** are the lowest energy tautomers that predominate in polar solvents. All three molecules can accept up to five hydrogen bonds using the two carbonyl oxygens and the N_9 nitrogen atom. Methylation reduces the number of hydrogen bonds that each can donate: Paraxanthine and theophylline can each donate one hydrogen bond, while caffeine can donate none. These molecules, which have similar, sub-ps rates of UIC,[4] were chosen to explore the effects of solute-solvent hydrogen bonding on vibrational relaxation.

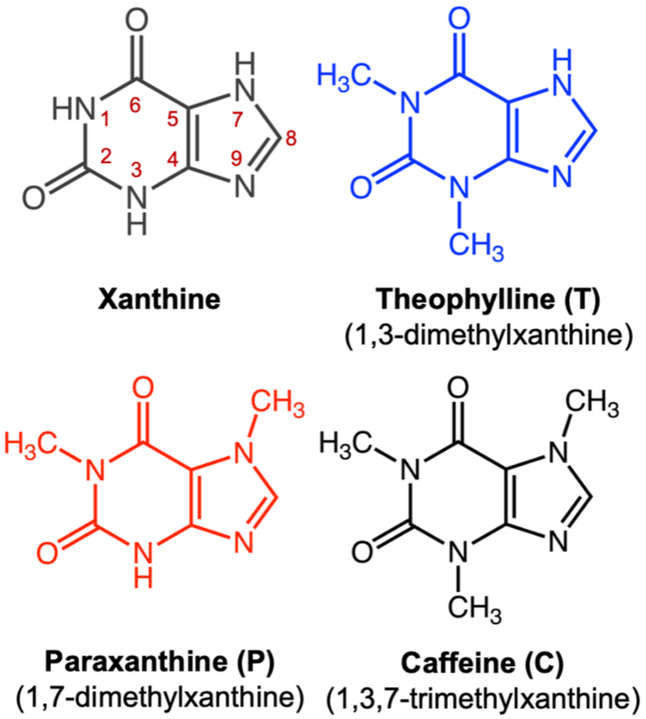

Figure 1. Structures of xanthine and the methyl-substituted derivatives studied. Atom positions are numbered for each compound as shown for xanthine.

A. Linear IR and DFT Calculations

Fig. 2 compares the experimental and theoretical linear IR spectra in the double-bond stretching region (*ca.* 1500-1750 cm^{-1}) for caffeine, paraxanthine, and theophylline dissolved in acetonitrile (CH_3CN) or heavy water (D_2O). D_2O was used instead of H_2O because of the former solvent's greater transparency in our spectral window. The spectra provide insight into methylation and solvent effects on the observed vibrational resonances. In CH_3CN, four bands are seen for all three molecules, which we refer to as bands 1-4 from high to low frequency. Band numbers for a specific compound will be preceded by C, P, or T for caffeine, paraxanthine, and theophylline, respectively. The experimental frequencies of the four bands of interest are listed in **Table I**.

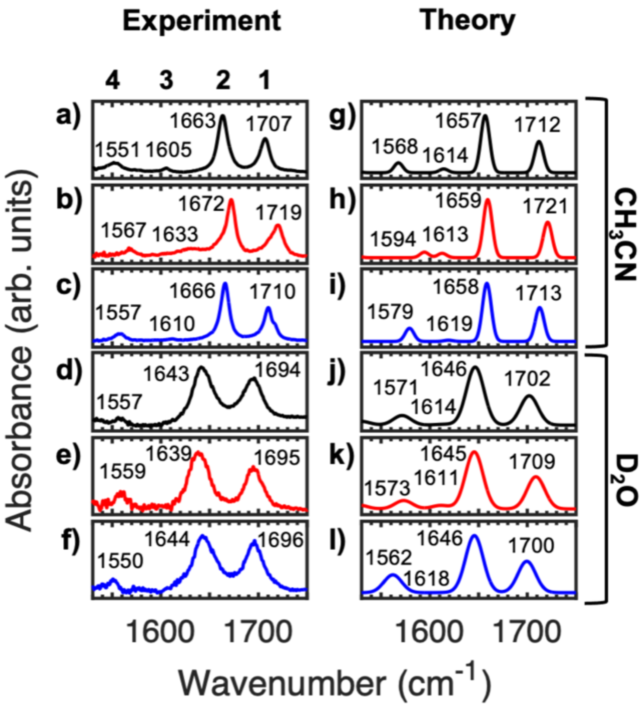

Figure 2. Linear IR absorption spectra of caffeine (black), paraxanthine (red), and theophylline (blue) in CH_3CN (uppermost six panels) and D_2O (lowermost six panels). (**a-f**) Experimental and (**g-l**) calculated normal mode spectra. Calculated peak lineshapes were generated by convoluting stick spectra with an area-normalized Gaussian with a FWHM of 7.5 cm^{-1} (CH_3CN) or 15 cm^{-1} (D_2O). The band index discussed in the text is shown just above panel a. The peak frequency in wavenumbers is indicated next to each band.

All three molecules have two intense, higher energy transitions (bands 1 and 2) and two weakly allowed lower frequency transitions (bands 3 and 4). Band 3 is weak in CH_3CN and virtually absent in D_2O solution. Upon going from CH_3CN (**Fig. 2a-c**) to D_2O (**Fig. 2d-f**), bands 1 and 2 downshift by *ca.* 10-30 cm^{-1} and the band full-width at half-maximum (FWHM) nearly doubles for all three molecules. Larger downshifts of 24 cm^{-1} and 33 cm^{-1} are observed for the P1 and P2 bands of paraxanthine, which lacks a methyl group at the N_3-position. Bands P4 and T4 exhibit a minor downshift of a few wavenumbers in D_2O as compared to CH_3CN, while C4 blue-shifts by approximately 6 cm^{-1}.

To interpret the molecular origins of the spectral features observed in the linear IR absorption spectra, DFT normal mode calculations were performed, as described in the methods section. Optimized bond distances are listed in **Table S2**. The distances calculated for caffeine are consistent with calculations for caffeine by Singh et al.[30] using the same level of theory. For comparison with experimental spectra, the calculated frequencies of the modes responsible for bands 1-4 (**Fig. S1-S3**) were convoluted with area-normalized Gaussians with a FWHM of 7.5 and 15 cm^{-1} for CH_3CN (**Fig. 2g-i**) and D_2O (**Fig. 2j-l**), respectively. The calculated linear IR spectra (**Fig. 2g-l**) agree very well with experiment (**Fig. 2a-f**). The calculated frequencies (no scaling was done) agree very well with the experimental ones, and the calculated intensities accurately capture the relative intensities of the four bands.

The calculated atomic displacement vectors shown in **Figs. S1-S3** (Supplementary Material) were used to make the normal mode assignments listed in **Table I**. These assignments suggest that delocalized vibrational modes give rise to bands 1-4 in all three molecules. The major character of the mode responsible for band 1 ("mode 1") involves symmetric stretching of the two carbonyl groups along with bending of the methyl groups on the pyrimidine ring. For paraxanthine and theophylline, there is an additional contribution from N_3-H(D) and N_7-H(D) wagging, respectively. The normal mode character is essentially the same for calculations in CH_3CN and D_2O. Mode 2 involves asymmetric stretching of the carbonyl groups accompanied by distortions of the pyrimidine ring. Modes 3 and 4 involve ring mode vibrations for all three molecules. Mode 3 is primarily localized on the pyrimidine ring with a major contribution from the C_4=C_5 stretch, while mode 4 is delocalized across both rings. To estimate the local stretching mode character of modes 1 and 2, the degree of delocalization of the normal modes was calculated from the relative norms of the displacement vectors in mass-weighted coordinates, following the procedure of Hamm et al.[31] The fractional contributions of the carbonyl local modes to mode 1 (and mode 2) are 69%, 66%, and 67% (65%, 67%, and 58%) in CH_3CN and 64%, 63%, and 63% (60%, 63%, and 46%) in D_2O for C, P, and T, respectively.

Table I. Experimental band frequencies of xanthine derivatives in CH$_3$CN and D$_2$O solution and DFT mode assignments.[a]

	Experimental		Theoretical
Mode	**$\tilde{\nu}_{\mathrm{CH_3CN}}$ (cm^{-1})**	**$\tilde{\nu}_{\mathrm{D_2O}}$ (cm^{-1})**	**Normal Mode Assignments**
C1	1707	1694	ν(C$_2$=O, C$_6$=O, symm), δ(N$_1$-CH$_3$), δ(C$_3$'-H$_3$)
P1	1719	1695	ν(C$_2$=O, C$_6$=O, symm), δ(C$_1$'-H$_3$), δ(N$_3$-D)
T1	1710	1696	ν(C$_2$=O, C$_6$=O, symm), δ(C$_1$'-H$_3$), δ(C$_3$'-H$_3$), δ(N$_7$-D)
C2	1663	1643	ν(C$_2$=O, C$_6$=O, asymm), ν(C$_4$=C$_5$), δ(C$_1$'-H$_3$), δ(C$_3$'-H$_3$),
P2	1672	1639	ν(C$_2$=O, C$_6$=O, asymm), ν(C$_5$=C$_6$), δ(N$_3$-D)
T2	1666	1644	ν(C$_2$=O, C$_6$=O, asymm), ν(C$_4$=C$_5$), δ(C$_1$'-H$_3$), δ(C$_3$'-H$_3$), δ(N$_7$-D), δ(C$_8$-H)
C3	1605	-	ν(C$_4$=C$_5$), δ(C$_3$'-H$_3$), δ(C$_8$-H), Py
P3	1633	-	ν(C$_4$=C$_5$), δ(N$_3$-D), δ(C$_7$'-D), δ(C$_8$-H), Py
T3	1610	-	ν(C$_4$=C$_5$), ν(C$_6$=O), δ(C$_3$'-H$_3$), δ(N$_7$-D), δ(C$_8$-H), Py
C4	1551	1557	ν(C$_4$=C$_5$), δ(C$_1$'-H$_3$), δ(C$_3$'-H$_3$), δ(C$_8$-H), Py + Im
P4	1567	1559	ν(C$_4$=C$_5$), δ(C$_1$'-H$_3$), δ(N$_3$-H/D), δ(C$_7$'-H$_3$), δ(C$_8$-H), Py
T4	1557	1550	ν(C$_4$=C$_5$), δ(C$_1$'-H$_3$), δ(C$_3$'-H$_3$), δ(N$_7$-D), δ(C$_8$-H), Py + Im

[a] Peak positions were obtained by fitting the experimental linear IR spectra to a linear combination of Voigt profiles. Symm (symmetric); asymm (asymmetric); ν (stretch); δ (bend); Py (pyrimidine ring); Im (imidazole ring), C$_i$' (carbon atom of methyl group at atom N$_i$ in Fig. 1).

B. Two-Dimensional Infrared (2D-IR) Spectroscopy

Polarization-resolved 2D-IR spectra of caffeine, paraxanthine, and theophylline were collected in acetonitrile (**Fig. 3**) to quantify the anharmonic couplings between the double-bond stretching modes that are required for IVR among solute modes.[13] At each waiting time, t_2, the absorptive 2D-IR spectra, $S_{2D}(\omega_1, \omega_3; t_2)$, contain pairs of oppositely signed negative (red) and positive (blue) peaks, which constitute a two-dimensional correlation map between the excitation (pump) frequency, $\omega_1/2\pi c$ (first pulse, vertical axis), and detection (probe) frequency, $\omega_3/2\pi c$ (third pulse, horizontal axis).[28,32] Hereafter, peak pairs in the 2D-IR spectrum will be referred to by the tuple (X, Y), where X and Y are band numbers (1 – 4) from the linear IR absorption spectra that represent the pump and probe frequencies in the 2D-IR spectra (i.e., $\omega_1/2\pi c$ and $\omega_3/2\pi c$ in **Fig. 3**), respectively.

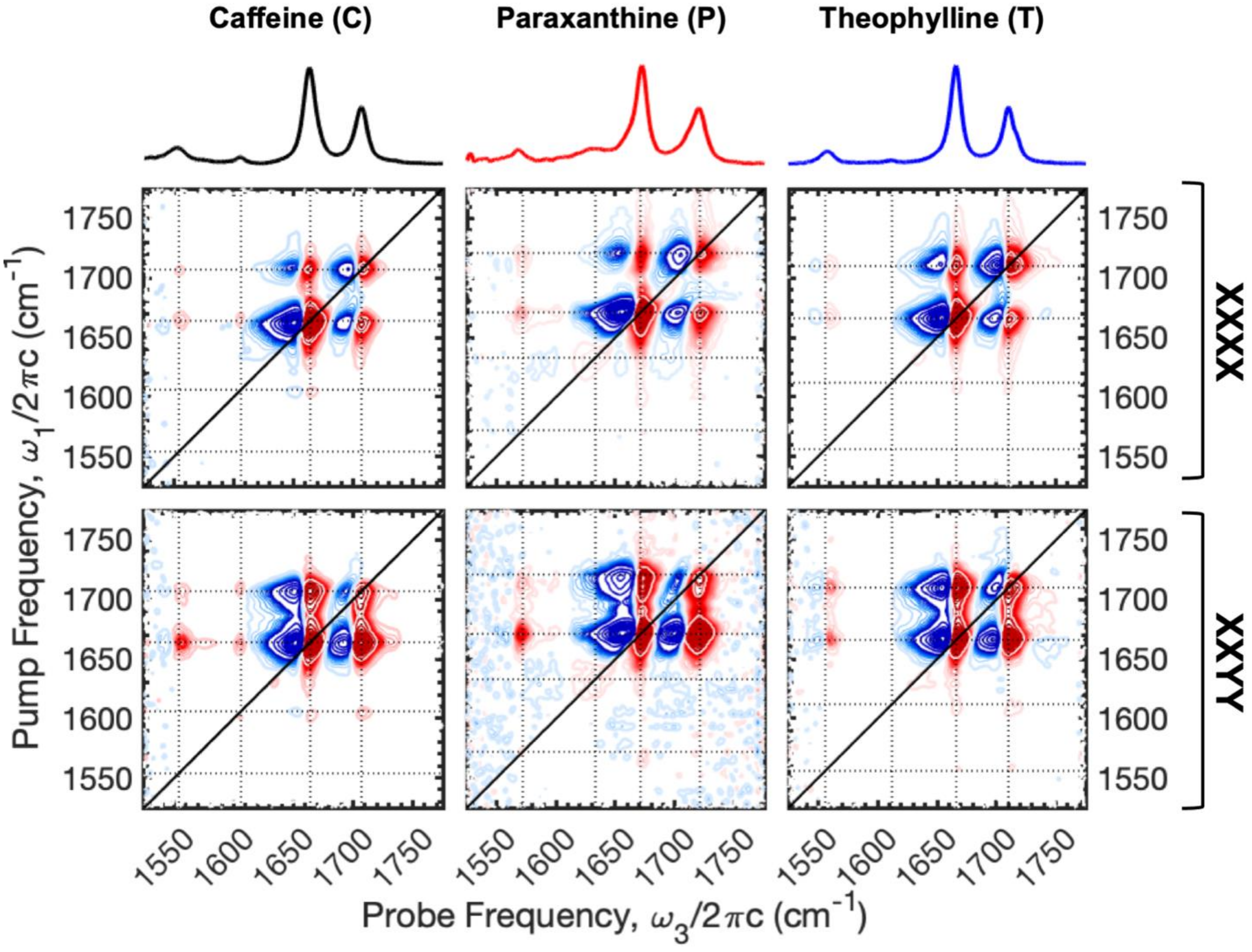

Figure 3. Polarization-resolved 2D-IR spectra of xanthine derivatives in CH_3CN at a waiting time of t_2 = 100 fs. Parallel (XXXX) polarization spectra are shown in the top row; perpendicular (XXYY) polarization spectra are shown in the bottom row. (Left column) caffeine, (center column) paraxanthine, and (right column) theophylline. Experimental linear IR spectra are shown above the 2D-IR spectra for convenience. Horizontal and vertical lines are drawn at the frequencies of the band maxima in the linear IR spectra (shown above

each column) as an aid to identifying cross peaks. Contour lines were drawn as described in the Method section (V).

The diagonal peaks involve pathways that excite the same vibrational mode, k, with the first and third laser pulses: The negative-going peaks involve excitation of the $\nu_k = 0$ to $\nu_k = 1$ transition with the excitation and detection fields, while the positive-going diagonal peaks involve excitation of the $\nu_k = 0$ to $\nu_k = 1$ transition with the excitation field and the $\nu_k = 1$ to $\nu_k = 2$ transition of the same vibrational mode with the detection field. The downshift of the $\nu_k = 1$ to $\nu_k = 2$ transition along the detection axis measures the on-diagonal anharmonic coupling, Δ_{kk}. Cross peaks involve pathways that excite two different vibrational modes, j and k, with the first and third laser pulses. In a system of coupled oscillators, the negative-going cross peaks involve excitation of two different $\nu_i = 0$ to $\nu_i = 1$ transitions, both to the 1-quantum manifold (see **Fig. S18** for an example of two coupled oscillators), while the positive-going cross peaks involve excitation of a $\nu_j = 0$ to $\nu_j = 1$ transition of mode j followed by excitation of a $\nu_k = 0$ to $\nu_k = 1$ transition of a different mode $k \neq j$ and access the 2-quantum manifold. The downshift of the positive cross peak by Δ_{jk} is a direct consequence of anharmonic coupling among two different modes through mixed-mode anharmonicity because the transition frequency of the $\nu_k = 0$ to $\nu_k = 1$ transition (measured by the third pulse) depends upon the excitation level of the anharmonically coupled mode j excited with the first pulse. By controlling the polarization of the laser pulses, one can measure the tensorial responses to obtain structural information.[28,32–34]

The 2D-IR spectra recorded at a waiting time of 100 fs are similar for all three molecules (**Fig. 3**). The two-dimensional line shapes are homogeneously broadened, as indicated by the diamond-shaped contours. A rich pattern of cross peaks is observed for all three molecules, confirming that the double-bond stretching modes are anharmonically coupled. For all three molecules, cross peaks are observed between all transitions for both polarization conditions, except between modes 3 and 4. In addition, the cross-to-diagonal peak ratios, which were calculated from the minimum signal amplitudes of the negative-going signals (red in **Fig. 3**) between modes 1 and 2, are three times more intense for perpendicular (XXYY) compared to parallel (XXXX) polarizations for each compound. The cross-to-diagonal peak ratios between modes 1 and 4 as well as modes 2 and 4 are also enhanced under perpendicular polarization conditions by a factor of 1.6 to 2.4 times, respectively.

To quantify the on- and off-diagonal anharmonic couplings, constant ω_1-slices through the 2D-IR datasets were taken for XXYY polarizations and fit to a linear combination of Voigt profiles using a least-squares fitting routine (**Figs. S4-6**). On- and off-diagonal anharmonic shifts were obtained from these fits using the procedure described in Supplementary Material Section S2. The results of the fits are summarized in **Table S3**. The peak fitting reveals similar on- and off-diagonal anharmonic peaks shifts of between 10 and 20 cm^{-1} for peaks (1,1), (1,2), (1,4), (2,1), (2,2) and (2,4) in all three xanthine derivatives. The remaining peaks were not fit due to the small signal amplitudes.

C. IR-PP Spectroscopy

IR-PP spectra were measured for parallel (XXXX) and perpendicular (XXYY) polarization conditions. The linearly polarized pump pulse bleaches an anisotropic distribution of molecules based on their alignment with the polarization direction of the pump pulse. A linearly polarized probe pulse, which is delayed in time with respect to the pump pulse by t_2, then monitors population, reorientational and energy transfer dynamics. The isotropic (magic-angle) spectra, $S^{iso}(t_2, \omega_3)$, track population dynamics in the absence of reorientational diffusion and were calculated from the parallel and perpendicular signals using,[34,35]

$$S^{iso}(t_2, \omega_3) = \frac{1}{3}[S^{XXXX}(t_2, \omega_3) + 2S^{XXYY}(t_2, \omega_3)]. \qquad (1)$$

The polarization anisotropy, $r(t_2, \omega_3)$, monitors the loss of correlation between an initially pumped transition dipole moment with a transition dipole moment probed after a time delay, t_2. The time-dependent anisotropy which captures orientational diffusion (or other depolarizing processes, such as energy transfer, that effectively rotate the probed transition dipole), is calculated as,[36,37]

$$r(t_2, \omega_3) = \frac{S^{XXXX}(t_2, \omega_3) - S^{XXYY}(t_2, \omega_3)}{S^{XXXX}(t_2, \omega_3) + 2S^{XXYY}(t_2, \omega_3)}. \tag{2}$$

The pump-probe spectra contain negative signals from ground state bleaching (GSB) and stimulated emission due to excitation of the $\nu = 0$ to $\nu = 1$ and de-excitation of the $\nu = 1$ to $\nu = 0$ vibrational transition, respectively, while positive signals arise from excited state absorption (ESA) of the $\nu = 1$ to $\nu = 2$ transition and are downshifted along the probe (ω_3) axis due to anharmonicity. Hereafter, we will describe the negative IR-PP signals as GSB signals for simplicity even though stimulated emission also contributes.

The isotropic IR-PP spectra of caffeine, paraxanthine, and theophylline are shown in **Fig. 4a, c, e** (CH_3CN) and **Fig. 4b, d, f** (D_2O) at various delay times. The early time spectra (**Fig. 4**) show similar features for all three molecules in each solvent. Each spectrum shows three (D_2O) or four (CH_3CN) oppositely signed pairs of bands. In both solvents, the center frequencies of the $\nu = 0$ to $\nu = 1$ transitions responsible for the negative bands do not change appreciably with time; however, the positive (ESA) bands arising from the $\nu = 1$ to $\nu = 2$ transitions of the carbonyl modes (modes 1 and 2) blue-shifts and narrow on the few ps timescale and are unchanged after ~5 ps in both solvents (**Fig. 4**). This is more readily seen in the normalized, isotropic IR-PP spectra for caffeine in CH_3CN (**Fig. S7**). In D_2O, the bands are broader and decay faster than in CH_3CN. The isotropic transient spectra recorded in CH_3CN decay to the baseline in tens of ps. In contrast, the spectra in D_2O decay to a broad negative difference spectrum (**Fig. 4**), which is assigned to heating of the solvent. Because of liquid D_2O's broad bend + libration combination band (band maximum at 1550 cm^{-1}),[38] approximately 90% of the pump pulse is absorbed by the solvent (**Fig.**

S8a), and this direct excitation is responsible for most of the solvent heating. The transient spectra no longer change after approximately 15 ps and agree well with the temperature-difference spectrum of hot D_2O published in ref. [39] (**Fig. S8b**).

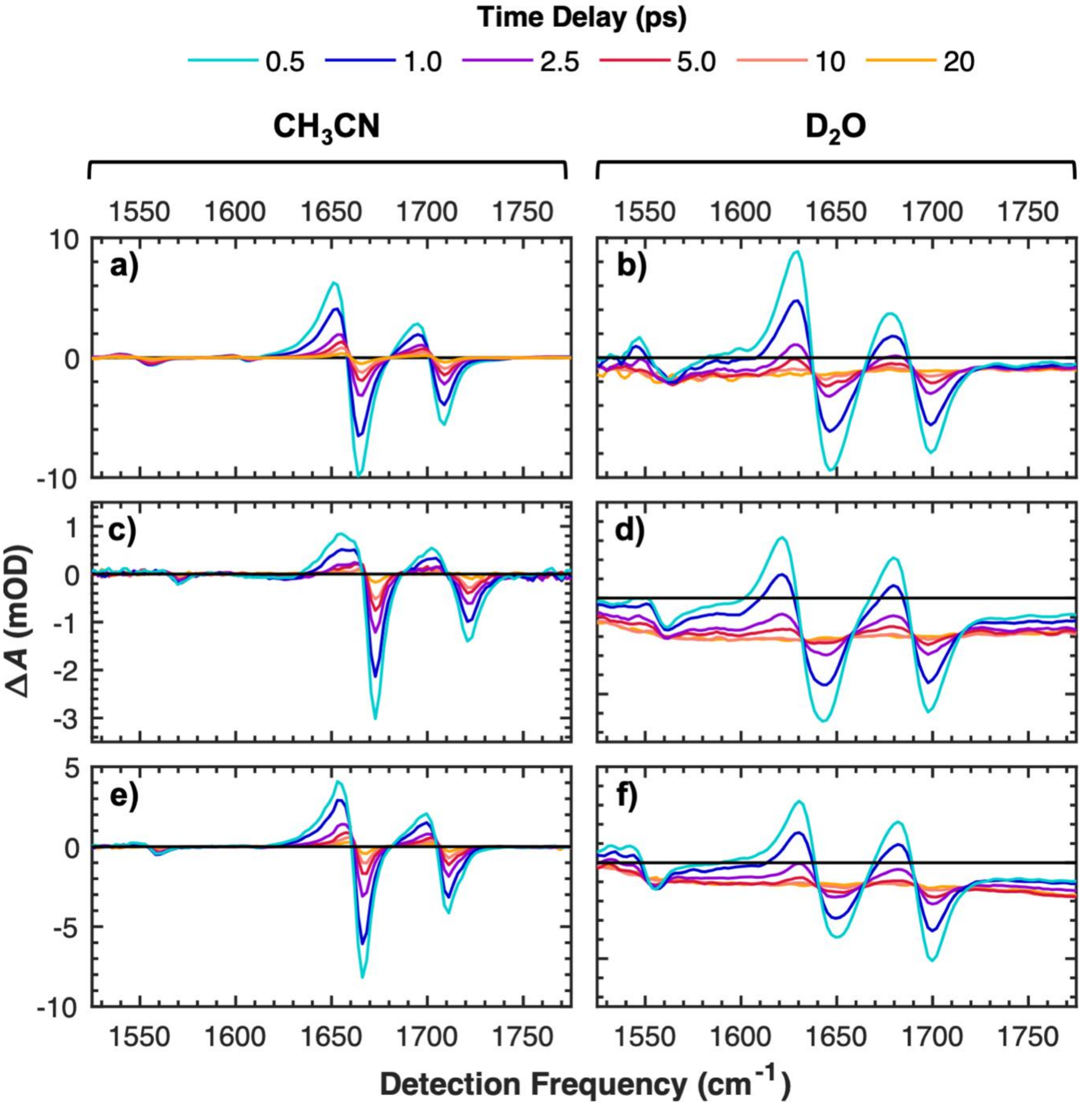

Figure 4. Isotropic infrared pump-probe spectra at various delay times in CH_3CN (left column) and D_2O (right column). **(a, b)** caffeine, **(c, d)** paraxanthine, and **(e, f)** theophylline. Signals were acquired with broadband pump and probe pulses centered at *ca*. 1640 cm^{-1}.

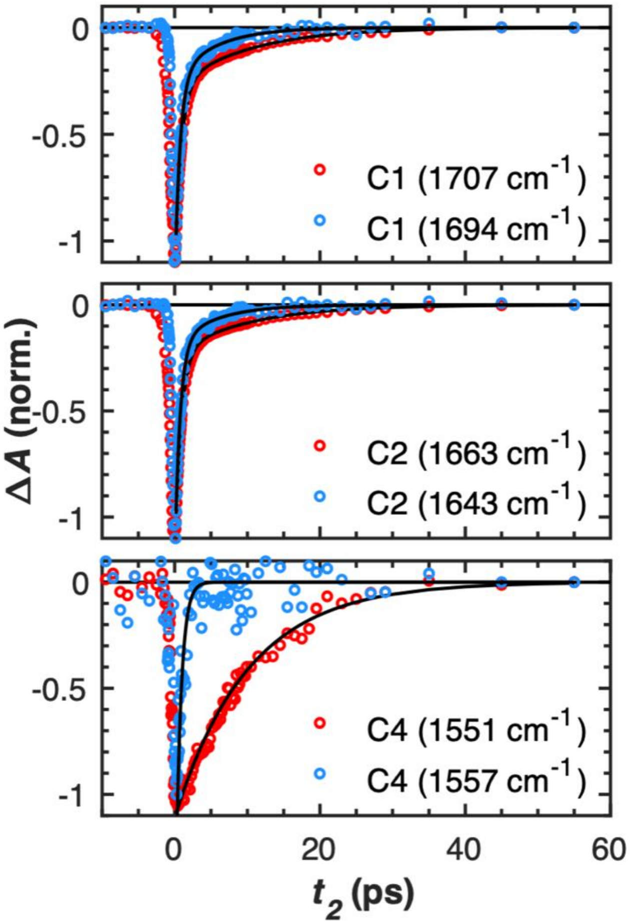

Figure 5. Normalized, kinetic traces at the indicated frequencies selected from the isotropic pump-probe signals in Figure 4 for caffeine in CH_3CN (red) and D_2O (blue). Bleach recovery kinetics at the indicated frequencies are shown for the C1 (top), C2 (middle) and C4 (bottom) bands together with global fits (solid lines) made to the full pump-probe data set. The best-fit parameters are summarized in Tables II and S4.

The isotropic signals, $S(t_2, \omega_3)$, in **Fig. 4** were globally fit to a biexponential function of the delay time t_2,

$$S(t_2, \omega_3) = a_1(\omega_3) \exp\left(-\frac{t_2}{\tau_1}\right) + a_2(\omega_3) \exp\left(-\frac{t_2}{\tau_2}\right), \quad (3)$$

where τ_1 and τ_2 are global time constants and a_1 and a_2 are detection-frequency dependent amplitudes. The carbonyl bands 1 and 2 were fit using both exponential terms, while only the second term was used to fit the signals for ring bands 3 and 4. The Akaike Information Criterion (AIC)[40] was used to determine the number of exponential terms used to fit each kinetic trace. Detailed explanation of the global fitting procedure and removal of the removal of the solvent-heating contribution in D_2O can be found in Section S3 of the Supplemental Material. The results of the global fit are shown in **Fig. S9** for caffeine in CH_3CN (paraxanthine in D_2O) as an example of the best (worst) global fits in the set of fits performed.

The GSB recovery kinetics corresponding to the maxima of bands 1, 2, and 4 (see **Table I**) of caffeine in CH_3CN and D_2O are illustrated in **Fig. 5**. Normalized traces for modes 1 – 4 of all three compounds are shown in **Fig. S10**. There is a stark difference in the bleach recovery kinetics of the carbonyl bands 1 and 2 vs. the ring modes 3 and 4. The isotropic signals for the carbonyl bands 1 and 2 are described by biexponential decays, with approximately 70-80% (see **Table S4**) of the carbonyl band signals decaying with a time constant (τ_1) of approximately 0.7-1.1 ps in CH_3CN or 0.6-0.7 ps in D_2O and the remaining signal decaying with a slower time constant (τ_2) of approximately 10-11 ps in CH_3CN and 3-5 ps in D_2O (**Table II**). Furthermore, the time constants observed are very similar for the three compounds and depend sensitively on the solvent. The ring mode signals lack the fast, τ_1-component ($a_1 = 0$) and instead are best described by a single exponential decay with the same τ_2 lifetime used to fit the carbonyl stretching modes (**Table II**).

Table II. Best-fit parameters from global fitting isotropic IR-PP kinetics.[a]

Molecule	**Solvent**	**τ_1 (ps)**	**τ_2 (ps)**
Caffeine	CH_3CN	0.86 ± 0.01	10.1 ± 0.1
	D_2O	0.72 ± 0.03	5.5 ± 0.6
Paraxanthine	CH_3CN	0.77 ± 0.02	10.3 ± 0.3
	D_2O	0.74 ± 0.03	4.3 ± 0.1
Theophylline	CH_3CN	1.14 ± 0.01	10.8 ± 0.2
	D_2O	0.61 ± 0.02	3.3 ± 0.1

[a] All uncertainties are $\pm 2\sigma$. Carbonyl modes (1 and 2) were fit to a biexponential function with time constants τ_1 and τ_2, while simultaneously fitting the transients for ring modes (3 and 4) to a monoexponential function with the same (global) τ_2 time constant.

To better understand the origins of biphasic relaxation, 2D-IR spectra were recorded as a function of waiting time, t_2, from 0.1 ps to 10 ps (**Fig. S12**) for caffeine in CH_3CN under XXXX polarization. The IR-PP spectrum is related to the 2D-IR spectrum by integration of the latter over the ω_1-axis (projection-slice theorem),[41] and thus the 2D-IR spectrum can resolve pathways induced by the pump pulse. At the earliest waiting time (0.1 ps), the energetically downhill ($\omega_1 > \omega_3$) cross peaks between the ring and carbonyl modes are similar in magnitude to the uphill ($\omega_1 < \omega_3$) cross peaks, with the downhill peaks being only marginally more intense than the uphill peaks (**Fig S7a**). As the waiting time increases through 2 ps (**Fig. S7d**), the downhill cross peak amplitude grows in relative to the uphill cross peak, and by the longest waiting time acquired (10 ps, **Fig. S7f**), the downhill cross peaks are much more pronounced than the uphill ones.

The observed waiting time-dependence of the uphill and downhill cross peaks is a signature of vibrational exchange among ring and carbonyl modes. To minimize the contribution of orientational diffusion and population relaxation, the ratio of the downhill cross-peak volume to diagonal peak volume (cross-to-diagonal peak ratio from here onwards) is plotted in **Fig. 6** as a function of waiting time. A kinetic model for incoherent population transfer among anharmonically coupled ring and carbonyl modes is discussed more extensively in Supplemental Material Section S4. Numerical solutions to the rate equations in **Eq. S2** are plotted as smooth curves and the universal rate of downhill population transfer from carbonyl to ring modes is estimated to be $k_d \approx$ (3.5 ps)$^{-1}$.

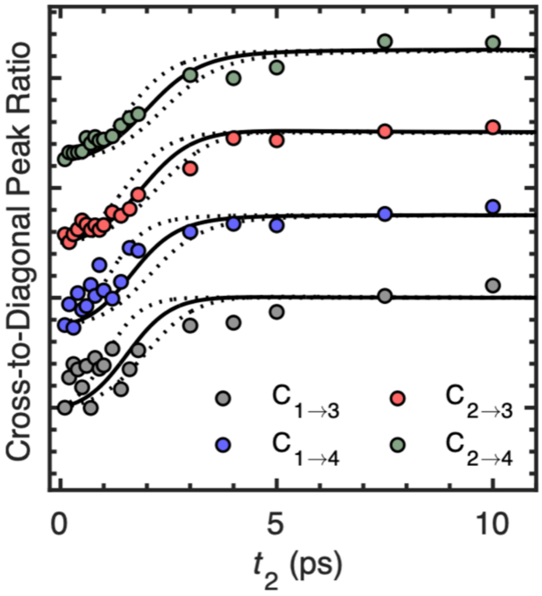

Figure 6. Cross-to-diagonal peak volume ratios for downhill population transfer from carbonyl (C1, C2) to ring (C3, C4) modes for caffeine in CH_3CN. Each data set was normalized at t_2 = 10 ps and displaced vertically for viewing. The black solid curve is the cross-to-diagonal peak ratio computed from **Eq. S2** using k_d = (3.5 ps)$^{-1}$. The upper and lower dashed curves correspond to k_d = (2 ps)$^{-1}$ and k_d = (5 ps)$^{-1}$, respectively. As a guide, the $C_{i\to j}$ cross-peaks are labeled in the 2D-IR spectrum in Fig. S12f.

Quantum beats, which are more prominent for band 1 than for band 2, are seen in the time-dependent anisotropy signals (**Fig. 7**) measured in CH_3CN solutions for bands 1 and 2 at the frequencies listed in **Table I**. Beats are also detected in the parallel- and perpendicular-polarization pump-probe signals (**Fig. S11**) but are not seen in the isotropic signals (**Fig. 5**). The initial anisotropy of band 1 is close to 0.1 and oscillates about the baseline, while band 2 shows an initial anisotropy of 0.3, which oscillates and decays. Band 1 also exhibits larger amplitude oscillations compared to band 2. The anisotropy of bands 3 and 4 were not investigated due to the low signals. Anisotropy decays for bands 1 and 2 were fit to a damped cosine (**Eq. 4**) and a mono-exponential decay plus a damped cosine function (**Eq. 5**), respectively,

$$S(t_2;\omega_3) = a_1 \exp\left(-\frac{t_2}{\tau_\mathrm{d}}\right)\cos(2\pi c\tilde{\nu}_\mathrm{osc}t_2 + \phi) + c_0 \tag{4}$$

$$S(t_2;\omega_3) = a_1 \exp\left(-\frac{t_2}{\tau_\mathrm{d}}\right)\cos(2\pi c\tilde{\nu}_\mathrm{osc}t_2 + \phi) + a_2 \exp\left(-\frac{t_2}{\tau_3}\right) + c_0, \tag{5}$$

where τ_d is the damping time constant, τ_3 is the time constant of the exponential decay, $\tilde{\nu}_\mathrm{osc}$ is the frequency of the oscillations in units of cm^{-1}, a_1 and a_2 are amplitudes, c_0 accounts for the constant signal offset and ϕ is the phase offset. The fit parameters for the signals shown in **Fig. 7** are summarized in **Table III**.

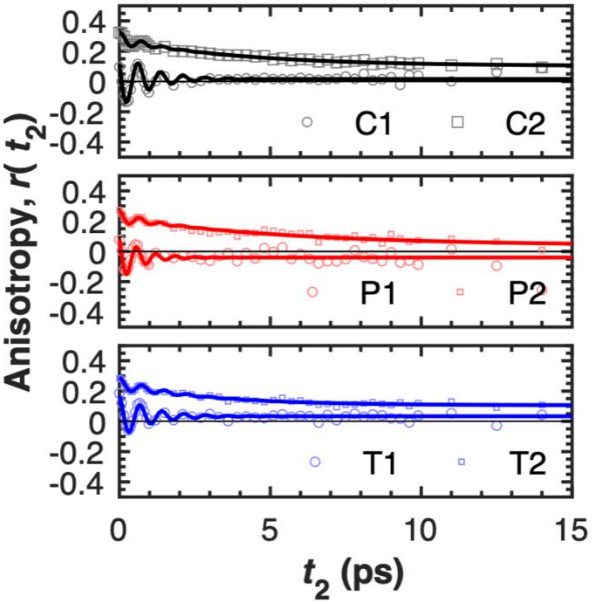

Figure 7. Anisotropy decays for the carbonyl modes of caffeine (black curves), paraxanthine (red), and theophylline (blue) in CH_3CN. Mode 1 is indicated by open circles, while mode 2 is indicated by open squares. Fits to the data are shown by solid lines. Every third data point is shown for clarity. Anisotropy decays are shown at the center frequencies in the linear IR spectra listed in Table I (C1 = 1707 cm^{-1}, C2 = 1663 cm^{-1}, P1 = 1719 cm^{-1}, P2 = 1672 cm^{-1}, T1 = 1710 cm^{-1}, and T2 = 1666 cm^{-1}).

Table III. Best-fit parameters for anisotropy signals in CH_3CN solutions.[a]

Molecule	Mode	τ_d (ps)	$\tilde{\nu}_\mathrm{osc}$ (cm^{-1})	τ_3 (ps)	c_0
Caffeine	1	1.0 ± 0.2	45 ± 1	-	0.016 ± 0.003
	2	0.7 ± 0.2	47 ± 1	4.2 ± 0.3	0.175 ± 0.004
Paraxanthine	1	0.7 ± 0.4	52 ± 4	-	-0.040 ± 0.007
	2	0.8 ± 0.6	48 ± 5	5.7 ± 1.3	0.185 ± 0.017
Theophylline	1	1.0 ± 0.2	46 ± 1	-	0.033 ± 0.003
	2	1.2 ± 0.5	44 ± 2	3.1 ± 0.4	0.140 ± 0.006

[a] Band 1 and 2 anisotropy signals were fit to eqs. 4 and 5, respectively.

III. DISCUSSION

A. Vibrational Mode Assignments

Based on the DFT calculations (**Table I**, **Fig. S1-S3**), we assign bands 1 and 2 in the caffeine, paraxanthine, and theophylline linear IR absorption spectra shown in **Fig. 2a-f** to the symmetric and asymmetric stretching vibrations of the C_2=O and C_6=O carbonyl groups, consistent with previous assignments.[30,42,43] Modes 1 and 2 are reduced in frequency and also broaden in D_2O as compared to CH_3CN (**Fig. 2**). Both effects are due to hydrogen bonding to D_2O molecules,[44] which increases the C_2=O and C_6=O bond lengths (**Table S2**) and results in inhomogeneous broadening. The shoulder on the blue edge of the T1 band in CH_3CN (**Fig. 2c**) is discussed in Section C below.

The calculations indicate that modes 3 and 4 are ring mode vibrations that are delocalized over the six-membered ring or both rings, respectively. The intensity of band 3 of each compound is calculated to be three to five times lower in D_2O than in CH_3CN (**Table S1**), consistent with the absence of this mode in the experimental spectra. Srivastava et al.[30] assigned caffeine's C3 band to C=C and C=N stretching, while the C4 band was assigned to imidazole ring stretching, C=N stretching, C=C stretching, and C-H bending, consistent with our DFT results (**Table I**).

The experimental linear IR absorption spectra (**Fig. 2a-e**), the DFT normal mode analysis (**Fig. 2g-l, Table I**), and the 2D-IR spectra (**Fig. 3**) indicate that each of the four modes in our detection window has largely the same character in all three xanthine derivatives studied. Methylating any two of the N_1, N_3, or N_7 atoms does not significantly change the atom displacements of the underlying normal modes (**Figs. S1-3**) or the pattern of anharmonic coupling (**Fig. 3**) between them. This contrasts with methylation of the pyrimidine nucleobase uridine 5'-monophosphate (UMP) at the C_5 position to yield thymidine 5'-monophosphate (TMP).[45] Wang et al. suggested that the methyl group of TMP hinders vibrational mode interactions by restricting charge flow, thus localizing the symmetric and asymmetric CO stretch of TMP relative to UMP.

H/D exchange at the N_3- and N_7-positions of paraxanthine, and theophylline, respectively, also minimally changes the normal mode character.[46] The Tokmakoff group showed that the local mode character of the amide II mode of *N*-methylacetamide isotopologues is quite sensitive to isotopic substitution and alters the degree of coupling among modes and vibrational relaxation timescales.[47] On the other hand, the amide I modes, which are dominated by C=O stretching (81-86% from PED analysis), were found to be less sensitive to isotopic substitution due to minimal contribution from groups with exchangeable protons.[47] A similar argument applies to the xanthines studied here, and we note that the $N_3H(D)$ and $N_7H(D)$ bending modes contribute negligibly to modes 1 and 2 of P and T, respectively. Summarizing this section, we note that neither the pattern of methylation nor H/D exchange significantly changes the character of vibrational modes 1 – 4, making them well suited for exploring how solute-solvent couplings affect vibrational relaxation in this family of compounds.

B. Coherent oscillations in the time-dependent anisotropy signals

Because relaxation and exchange processes act as dephasing mechanisms, the observation of coherent oscillations reports directly on the subset of molecules in the subensemble that have not exchanged during the t_2 waiting period.[48] Thus, before detailed analysis of the solvent-dependent vibrational relaxation dynamics can be considered, it is necessary to establish why coherent oscillations are observed in the anisotropy, parallel and perpendicular IR-PP signals, but not in the isotropic signals. When experiments are performed with broadband pump sources, such as those performed in the current study, additional pathways which evolve as coherences during t_2 (“interstate coherences”) can lead to modulations of the signals which beat at the difference in energy between the two states involved in the coherence (e.g., coherent oscillations) provided that the solute-solvent coupling is weak relative to the intramolecular coupling.[49,50]

The quantum beat in the anisotropy signals of bands 1 and 2 has the same frequency ($\tilde{\nu}_{\mathrm{osc}}$ in **Table III**) within experimental uncertainty and the beat frequency matches the frequency difference between bands 1 and 2 for each xanthine derivative (**Table I**), indicating that the symmetric and asymmetric carbonyl stretching modes experience coherent exchange of excitation. Earlier, vibrational population transfer dynamics between the symmetric and asymmetric stretching modes of the two carbonyls in the β–diketone 2-acetylcyclopentanone were studied by Park and Ji using 2D-IR spectroscopy.[51] They also observed identical vibrational population decays for both modes using IR-PP spectroscopy. Furthermore, the decays were biexponential with lifetimes of approximately 1.0 ps (70%) and 12 ps (30%), which closely mirror the current work. However, these authors saw no evidence of coherent population transfer in their experiments and suggested that very rapid dephasing results in incoherent population transfer.

To explain why coherent oscillations are seen in the anisotropy (**Fig. 6**) and parallel and perpendicular pump-probe signals (**Fig. S10**), but not in the isotropic signals (**Fig. 5**), we construct a simple model based on the nonlinear response of two coupled oscillators that represent the symmetric (mode 1) and symmetric (mode 2) carbonyl stretches. In the model presented in Supplementary Material Section S6, the polarization-resolved pump-probe signals are computed from the response functions (**Eq. S1-S6**) neglecting orientational diffusion, which occurs slowly compared to the damping of the oscillations (i.e., $\tau_3 > \tau_d$). Under the harmonic approximation, the orientational factors in the nonlinear response functions depend on the angle between the transition dipole moments (TDMs) of the symmetric (s) and symmetric (a) stretch modes, $\theta_{1,2}$ (**Table S5**). Of the 20 pathways that generate a pump-probe signal, only six pathways result in oscillatory signals (**Tables S6**). Importantly, the response functions vanish when the mixed-mode anharmonicity vanishes, indicating that the coherent oscillations in the pump-probe spectra are a direct consequence of anharmonic coupling.[52] Furthermore, these pathways are only present if the bandwidth of the pump pulse is broad enough to excite both transitions coherently.

The calculated anisotropy and pump-probe spectra under parallel, perpendicular, and magic-angle polarizations for various TDM angles are simulated in **Figs. S12-S13** at the ground-state bleach frequencies of bands 1 and 2, respectively. The simulations show that the oscillatory response of the isotropic signal vanishes when $\theta_{1,2} = 90^\circ$ as can also be seen from the equations in **Table S6**. The lack of oscillations in the isotropic pump-probe signals thus confirms that the TDMs of the symmetric and symmetric stretching modes are approximately orthogonal in their orientations. This agrees with the DFT calculations, which show that the angle between the TDMs of modes 1 and 2 is close to 90° (**Table S1**). This is also consistent with the enhanced cross-peak intensities seen in the 2D-IR spectra for perpendicular vs. parallel polarizations (**Figure 3**). Note that when two anharmonically coupled vibrations are approximately described by the symmetric and anti-symmetric linear combinations of two local modes with equal TDM magnitudes, as is the case here for the coupled carbonyl stretch vibrations of caffeine, then the resultant TDMs will be orthogonal regardless of the original angle between the TDMs of the uncoupled local modes provided that the uncoupled TDMs are noncollinear.[53]

DeFlores et al.[47] previously observed coherent oscillations in the broadband pump, isotropic IR-PP spectra of *N*-methylacetamide (NMA) isotopologues, NMA-h_7 and NMA-d_7 at the amide I and II transitions. By simultaneously fitting the parallel and perpendicular 2D-IR spectra, the authors derived a projection angle between the TDMs as 40° and 70°, respectively, which explains why the oscillations are well-resolved in their isotropic spectra. Further, the authors used the absolute value rephasing spectra to provide independent proof that the oscillatory signals in the isotropic pump-probe signals originated from coherent excitation of the amide I and II modes. In the current work, coherent excitation and subsequent dephasing of the symmetric and asymmetric carbonyl modes are unambiguously assigned by the presence or absence of coherent oscillations in the different polarization-resolved IR-PP measurements. We attempted to simultaneously fit the XXXX and XXYY 2D-IR spectra using an eigenstate-based model similar to the one used by DeFlores et al.[47] to derive projection angles between TDMs as was done previously for nucleobases.[45] However, the fitting resulted in large uncertainties in the predicted projection angles, which we explain by the weak ring mode signals and the large number of free parameters.

Wang and co-workers[54] observed coherent oscillations in the anisotropy decays of indigo carmine probed at the asymmetric carbonyl stretching and ring mode frequency, with little to no oscillations in the isotropic IR-PP signals. The authors attributed the ability to resolve oscillations in anisotropy to the fact that the population relaxation contribution is removed in anisotropy but did not consider how the anisotropy and isotropic signals depend upon the projection angle between TDMs. Our numerical results (**Fig. S15-16**) show that the anisotropy is only free from coherent oscillations and departs from the expected initial anisotropy value, $r(0) = 2/5$, when the projection angle between TDMs is 0° (parallel) or 180° (anti-parallel), while the isotropic signals are only free from oscillations when the projection angle is 90°. Although the authors did not provide the projection angle between TDMs, inspection of the atomic displacements (Fig. 1c therein) suggests that transition dipole moments would be close to perpendicular.

C. IVR Dynamics

Vibrational relaxation is frequently described statistically, whereby Fermi's Golden Rule (FGR) provides an expression for the rate of decay of an initial vibrational excitation to a dense manifold of states. In FGR, the rate of transfer is proportional to the product of an average coupling, $|V|^2$, between the initially excited state and manifold of states and the density of those states, $\rho(\omega)$, evaluated at the energy gap of the transition.[55] The Landau-Teller treatment of vibrational relaxation starts from FGR and includes the influence of the bath by including a "frictional" damping force proportional to a force-force autocorrelation function felt by the oscillator.[11] The spectral density of the solvent typically decays exponentially with increasing frequency, giving rise to the conventional wisdom that relaxation to the solvent proceeds through lowest-frequency solvent modes (roughly $k_B T$).[56] Precisely how much energy is taken up by the solute can vary from 100%, in which case vibrational relaxation is identical to "pure IVR", to 0%, in which case it is "pure IET". Some authors have proposed that IET and IVR proceed on similar timescales, and that medium- to high-frequency modes play an important role in vibrational relaxation.[18] Further, relaxation may proceed via mode-specific pathways, rather than statistical, in which a fast IVR step populates near-degenerate states coupled by low-order anharmonic interactions, followed by slower dissipation of excess vibrational energy.

The isotropic pump-probe signals, which are devoid of coherent oscillations and decay monotonically, monitor population relaxation dynamics without unwanted modulations from coherent oscillations. The two excited carbonyl modes 1 and 2 relax in unison in CH_3CN and D_2O for each xanthine derivative (**Table II**). The fast, τ_1-component of the biphasic decay is responsible for 68-80% (CH_3CN) and 71-84% (D_2O) of the total signal amplitude (**Table S4**). Ring modes 3 and 4 decay with a nearly identical long-time, τ_2-component, which accounts for 100% of the total signal decay. In the following, we discuss the intriguing observation of single- (ring) and biexponential (carbonyl) decays for these nearly isoenergetic vibrational modes. The fast component seen in the biphasic decay of the carbonyl mode signals (**Fig. 5**) is assigned to mode-specific, sub-picosecond IVR from the carbonyl modes to predominantly lower frequency solute modes other than the ring modes. This assignment is supported by downhill cross-peak analysis, transient blue-shifting of the ESA, and the damping of the anisotropy signals, as we discuss now in greater detail.

The waiting-time dependent 2D-IR spectra (**Figs. 6** and **S12**) provide clear evidence of downhill population transfer (IVR) from anharmonically coupled carbonyl to ring modes with a characteristic timescale of approximately 3.5 ps. Based on the 2D-IR analysis, the most straight-forward explanation for the common global decay of the IR-PP spectrum (dictated by τ_2) and the common solvent-dependent relaxation of the carbonyl and ring modes is direct relaxation from

CO to ring modes, where the bottleneck to thermalization is rate-limited by relaxation of the ring modes. However, this model fails to account for the discrepancy in timescales between the carbonyl-to-ring exchange (k_d^{-1} ≈ 3.5 ps) and fast decay of the carbonyl modes (τ_1 = 0.86 ps for caffeine, CH_3CN). Furthermore, if the carbonyl modes relaxed primarily to the ring modes, one would expect to see a fast growth on the timescale of τ_1, followed by a slower decay of the ring mode amplitudes; yet the IR-PP signals decay with a single exponential time-constant for all xanthine derivatives in both solvents. From the projection-slice theorem,[57] the IR-PP signals of the weakly absorbing ring modes should be particularly sensitive to population transfer from the strongly absorbing carbonyl modes since the carbonyl-to-ring mode cross peaks scale as $\propto |\mu_R|^2|\mu_{CO}|^2$, while the diagonal ring mode peaks scale as $\propto |\mu_R|^4$. The absence of any observable "growth, then decay" in the ring mode IR-PP signals can be understood by analysis of the downhill carbonyl-to-ring mode transfer timescales. By $t_2 = 3.5$ ps, the exponential-term from τ_1 has decayed to 1.7% of its maximum value (using parameters for caffeine in CH_3CN in **Tables II** and **S4**), thus explaining the absence of any relaxation-induced growth in ring mode signal amplitudes. From this analysis, it is concluded that the ring modes do not serve as primary IVR-accepting modes for the carbonyl modes; however, due to weak anharmonic coupling among them, exchange can be observed by careful inspection of the 2D-IR spectra (**Fig. S12**). We explain the fast relaxation of the carbonyl modes by IVR to anharmonically coupled modes of the solute or by direct population transfer to solvent modes.

The modest solvent-dependence of the τ_1-component indicates that the carbonyl modes undergo fast IVR to low-frequency solute modes. In D_2O, each carbonyl mode can form two hydrogen bonds from the solvent. Consequently, the carbonyl fundamental transition frequency (**Fig. 2**) is red-shifted relative to the non-bonded solute molecule due to the vibrational Stark effect.[58] Despite the strong solute-solvent coupling in D_2O, the τ_1-component (**Table II**) displays only a modest decrease of 16.3 ± 0.4% (caffeine) or 3.9 ± 0.5% (paraxanthine), compared to 45.5

± 0.6% (caffeine) 58.3 ± 0.2% (paraxanthine) for the τ_2-component when going from CH_3CN to D_2O. In theophylline, the τ_1-component, which is anomalously large in CH_3CN (see below) shows a greater decrease of 46.5 ± 0.2% compared to the 69.4 ± 0.1% decrease in τ_2. In both solvents, the amplitude of the fast component (a_1 in **Table S4**) remains largely unchanged, signifying that this pathway is present in both solvents. This, along with the modest solvent-dependence suggests that the τ_1-component originates predominantly from *intramolecular* relaxation.

Further support of IVR is provided by the transient blue-shift of the carbonyl mode ESA in the IR-PP spectra (**Fig. 4** and **Fig. S7**). The transient blue-shift observed in the IR-PP spectra originates from transient blue-shifts in the cross peak *only* in the 2D-IR spectra; this is explained in terms of an IVR model for anharmonic oscillators. The transient blue-shift in the IR-PP and 2D-IR spectrum can originate from several factors, including spectral diffusion, chemical exchange, and vibrational relaxation. To determine if the blue shifting in the IR-PP spectra originates from spectral diffusion, we look to the 2D-IR spectra of caffeine in CH_3CN (**Fig. S12**). The IR-PP spectrum at a given time delay, t_2, is related to the 2D-IR spectrum by integrating the latter along the pump frequency axis (projection-slice theorem).[41] The peak shapes of the diagonal peaks in the 2D-IR spectra in **Fig. S12** are circular in appearance at a waiting time of 0.1 ps and are essentially unchanged in shape at 1 ps. This indicates that the transient blue-shifting and narrowing seen in the IR-PP spectra is not due to solvent-induced fluctuations of the transition frequencies (spectral diffusion) and is consistent with homogeneously broadened lines. Further, spectral diffusion tends to broaden, rather than narrow, the line shape.[59] Hydrogen-bond making and breaking (a chemical exchange process) can also lead to transient blue-shifting; however, the magnitude of the blue-shift observed in the IR-PP is significantly smaller (< 5 cm^{-1}) than the shift due to hydrogen-bond formation (10-25 cm^{-1}, **Table I**). Heating of the local environment upon vibrational relaxation is also known to weaken intermolecular hydrogen bonds and result in transient blue-shifting.[44] Both processes are ruled out here because transient blue-shifting of the ESA is observed for caffeine in CH_3CN, which does not form hydrogen bonds with the solvent.

Instead, the transient blue-shifting of the ESA is best explained by IVR. Kubarych[60] and others have previously used the absolute value non-rephasing 2D-IR spectrum as a clean probe of IVR dynamics because, in the absence of IVR, cross-peak pathways evolve as ground state populations during t_2. In other words, any rise in the cross-peak amplitudes during t_2 reflects population transfer. Although it is possible to extract the non-rephasing spectrum from the absorptive 2D-IR spectrum by a Fourier transform as described by Ogilvie et al.[61], an approach based on the analysis of the absorptive 2D-IR spectrum would be desirable. Here, an alternative measure of IVR to low-frequency solute modes outside of the 2D-IR spectral window is presented for absorptive 2D-IR spectra. For a system of coupled (anharmonic) oscillators, the anharmonic transition frequency, $\nu(n_k \rightarrow n_{k+1}) = \nu_k$, of mode k depends on the number of quanta in the remaining vibrational modes, and is given by,[12]

$$\nu(n_k \rightarrow n_{k+1}) = \nu_k + 2x_{kk}n_k + \sum_{i \neq k} x_{ik}n_i \tag{6}$$

$$\nu_k = \omega_k + 2x_{kk} + \frac{1}{2}\sum_{i \neq k} x_{ik} \tag{7}$$

ν_k is the anharmonic transition frequency of the molecule at 0 K, ω_k is the harmonic frequency of mode k, x_{ii} and x_{ij} are on- and off-diagonal anharmonicity constants, and n_i is the quantum number of the i^{th} vibrational mode. In the absence of IVR during t_2 or at time delays $t_2 \ll \tau_{IVR}$, the on- and off-diagonal peaks shifts are given by $\Delta_{ii} = 2x_{ii}$ and $\Delta_{ij} = x_{ij}$ (an example double-sided Feynman diagram is found in **Fig. S18**). If IVR populates low-frequency solute modes during t_2, the on-diagonal frequency shift, Δ_{ii}, is unchanged, while the off-diagonal frequency shift is now $\Delta_{ij} = \sum_{i \neq j}(\tilde{n}_i - n_i)x_{ij}$, where n_i and $\tilde{n}_i$ are the vibrational quantum numbers of mode i before and after IVR, respectively. In other words, the IVR-induced change in transition frequency will shift the positively signed cross-peak position along the ω_3-axis, altering the mixed-mode anharmonic shift, Δ_{ij} (see *Results, Section B*).

Constant pump-frequency slices through the 2D-IR spectra of caffeine in CH_3CN at the C1 and C2 pump frequencies were normalized to the absorption maximum of the cross peak (**Fig. S17**) and compared with the IR-PP spectra (**Fig. S7**). Unlike the IR-PP spectra, in which transient blue-shifting is observed in both ESA features, only the cross peaks blue-shift with time, while the diagonal peaks decay with minimal frequency shifts. Using the projection-slice theorem, it is evident that the transient blue-shifts observed at the cross-peak locations in the 2D-IR spectra will appear in both ESA features, as described above. Although the anharmonicity constants, x_{ij}, are unknown, the sign[62] of x_{ij} can be positive or negative, and thus the population of low-frequency solute modes via IVR likely accounts for the reduced off-diagonal shift, because positive and negative x_{ij} will reduce the net magnitude of the shift. In a previous study[63] of $Rh(CO)_2$acac, the off-diagonal anharmonic shift was found to be twice that of the on-diagonal anharmonic shift (e.g., $\Delta_{AS} \approx 2\Delta_A \approx 2\Delta_S$), placing the relaxation-induced peaks in unique regions of the 2D-IR spectrum. In the current studies, very similar on- and off-diagonal shifts (**Table S3**) leads to strong overlap between relaxation-induced peaks and the cross peaks originating from anharmonic coupling, which complicates the analysis of the IVR process due to overlapping resonances. Nevertheless, the transient blue-shift observed in the 2D-IR and IR-PP spectra is attributed to IVR. A brief discussion of the transient blue-shift observed in mode-specific relaxation (this study) and its use as a probe of vibrational cooling following statistical relaxation (as in molecular thermometer) can be found in the Supplemental Material.

The anisotropy signal dynamics also point to rapid IVR. The anisotropy decays as a single exponential with time constant, τ_3, modulated by oscillations that are exponentially damped with a time constant τ_d (**Fig. 6, Table III**). For both the symmetric and asymmetric stretching modes, the initial anisotropy is less than the value of $2/5$ expected for a single oscillator. It is known that coherent superpositions of TDMs can produce initial anisotropy values that deviate from $2/5$.[64–66] The departure of the initial anisotropy values from $r(0) = 2/5$ is also evident in the modeling of coherent oscillations presented earlier (**Figs. S15-16**). The relative amplitude of the oscillations can be interpreted with help from the 2D-IR signals and projection-slice theorem. The anisotropy measured at the band 1 detection frequency has larger contributions from cross peaks than the diagonal peaks (**Fig. 3**). Conversely, band 2 is dominated by diagonal peaks, which reflect population dynamics, explaining the enhancement of the oscillations at the band 1 detection frequency.

We explain the damping of the coherent oscillations in the anisotropy by population relaxation due to rapid IVR by the carbonyl modes as seen by the transient blue-shifting of their ESA (**Fig. 4**). In CH_3CN, the time constant associated with damping of the coherent oscillations in the anisotropy signals (τ_d in **Table III**) agrees within experimental uncertainty with τ_1 of the isotropic signal decays in **Table II**. This suggests that the rapid τ_d decay is best explained by incoherent population relaxation from the $\nu = 1$ state of the carbonyl stretch modes to lower frequency modes via IVR. Decay due to reorientation of the excited molecules could also damp the coherent oscillations but is expected to occur more slowly. The anisotropy kinetics required fitting to a single exponential with an offset, suggesting that the loss of correlation due to molecular reorientation is incomplete on the timescale of vibrational relaxation. Anisotropy signals for the carbonyl mode of the carbonyl-containing aromatic compound isoniazid were also found to decay due to vibrational energy transfer and not molecular rotation.[67] In D_2O, τ_d is roughly 3-fold shorter than τ_1 (**Table II**) for caffeine, suggesting that the dephasing has a larger contribution from solvent fluctuations than in CH_3CN (**Fig. S11**). DeFlores et al. observed similar timescales for damping of coherent oscillations for NMA-d_7 in D_2O.[47] Wang and co-workers observed coherent oscillations in the anisotropy of indigo carmine in DMSO that decay with a time constant of 2 ps.[54] They assigned this decay to molecular reorientation, but this likely too fast for a molecule of this size.

For these reasons, we believe that our use of two distinct exponential time constants (τ_d and τ_3, **Table III**) is most consistent with the underlying physical processes, and that damping of the coherent oscillations is dominated by population relaxation.

The ring and carbonyl stretch modes might be expected to undergo IVR at similar rates because their vibrational quanta differ by a modest amount (~10%) that is on the order of thermal energy ($k_B T$), suggesting that the density of accessible states varies minimally for ring and carbonyl modes. It is thus puzzling why the nearly isoenergetic ring modes do not exhibit a fast IVR component. Although conventional treatments of IVR in the condensed phase posit that the density of states significantly changes IVR rates compared to the gas phase,[68] IVR rates depend not only on energy gaps and state densities but also on the anharmonic couplings to energetically accessible states. The vibrational mode character of the ring and carbonyl modes differs greatly (see above), making it likely that the pattern of anharmonic coupling to low-frequency solute modes also differs for each. To assess whether the number of IVR-accessible states differs significantly between the ring and carbonyl modes, a tier model based on low-order intramolecular coupling was considered as described in Section S7 of the Supplementary Material. This model suggests that the density of low order coupled states is not the primary determinant of IVR by the ring or carbonyl modes and instead implicates specific mode couplings among a few strongly coupled states.

Further evidence that mode-specific (anharmonic) couplings – rather than the density of coupled states – determine IVR rates comes from the decelerated rate of IVR for theophylline in CH_3CN. The value of τ_1 of theophylline is 30-50% larger than τ_1 of caffeine and paraxanthine (**Table II**), despite the minimal changes to both the normal mode character and similar on- and-off diagonal anharmonic couplings (**Table S2**) among the ring and carbonyl modes. The τ_1 values in **Table II** show no trend with molecular size. According to traditional theories of IVR, caffeine with 66 vibrational degrees of freedom compared to 57 each for paraxanthine and theophylline should have the smallest τ_1 in both solvents. However, in CH_3CN, τ_1 decreases as T (1.14 ps) >

C (0.86 ps) > P (0.77 ps), while in D_2O, the opposite trend is observed, P (0.74 ps) > C (0.72 ps) > T (0.61 ps). Although the number of low-order states is consistently smaller for theophylline than paraxanthine and caffeine (**Fig. S19**), this is true in both solvents (CH_3CN and D_2O), and thus cannot explain the solvent-dependent τ_1 lifetime in CH_3CN. These observations suggest that the mode-specific couplings that facilitate IVR are somehow altered for theophylline in CH_3CN.

The anomalous IVR lifetime of T1, T2 in CH_3CN suggests that N_7-deuteration and/or solvent-specific interactions accelerate IVR by theophylline in D_2O through resonant IVR pathways. It is well known that frequency shifts, either due to isotopic substitution or solvatochromism, can tune or detune resonant pathways for IVR.[20,21,69] Solute-isotope effects can change the character of a vibrational mode by altering the contributing atom displacements. As established above, however, the normal mode character changes minimally for all four modes of interest with deuteration. Further, it appears that the increased IVR lifetime is correlated with the presence of a weak shoulder on the blue edge of the T1 peak in CH_3CN (**Fig. 2c**). This feature, which is absent for theophylline in D_2O and for caffeine and paraxanthine in both solvents, is not captured by normal mode calculations. Together, these observations point to a weakly allowed combination band, overtone band, or a Fermi resonance, which arises from anharmonicity. Although Fermi resonances are often associated with an increase[20,21,47] in IVR rates, Kubarych and co-workers provided a counter example, where Fermi resonances hindered vibrational relaxation in $Mn_2(CO)_{10}$.[60] A more definitive assignment is beyond the scope of this work, but the evidence suggests that the number of accessible resonant IVR pathways is altered even though the normal mode character and anharmonic couplings among ring and carbonyl modes remain unchanged.

D. Solvent-Dependent Population Relaxation of Carbonyl and Ring Modes

We next discuss the origin of the slow phase of vibrational relaxation, which is unaffected by solute-isotope effects. The most intriguing observation is that vibrational relaxation of the ring and carbonyl modes in both solvents can be characterized by a global time constant (τ_2, **Table 2**), despite their very different initial vibrational dynamics and mode character. **Fig. 8** summarizes the solvent-dependent vibrational relaxation of the carbonyl and ring modes in CH_3CN and D_2O. Mono-[70–72] and biexponential[47,51,54,73–75] decays have been reported previously for carbonyl modes in both protic and aprotic solvents. However, comparatively few studies[54,76] have reported vibrational lifetimes for ring modes, likely due to their smaller cross sections, and to our knowledge, no studies have reported mono- and biexponential decays for ring and carbonyl modes in the same molecule.

One possible explanation for the global τ_2 lifetime of the IVR intermediate states and the ring modes is that relaxation is not mode specific, but closer to the statistical limit. This would give rise to a monotonic population decay whose rate is described by Fermi's Golden Rule.[77] Strong evidence for statistical relaxation of the ring modes was provided in the previous section. The 2-3-fold decrease in τ_2 from CH_3CN to D_2O is consistent with access to additional low-frequency modes of the solute-solvent complex (typically in the range of 50-300 cm^{-1}) upon hydrogen bonding.[44] For example, Tominaga and co-workers showed that the rate of VER for the carbonyl stretch of acetic acid in methanol and 2-propanol is accelerated by 60-80% for each additional hydrogen bond formed.[78] However, the total number of hydrogen bonds formed between the solute and solvent cannot alone explain the trend in τ_2 across the series of xanthines in CH_3CN and D_2O (**Table 2**). In CH_3CN, τ_2 is the same within experimental uncertainty, while in D_2O, τ_2 decreases according to caffeine (5.5 ± 0.6 ps) > paraxanthine (4.3 ± 0.1 ps) > theophylline (3.3 ± 0.1 ps). Paraxanthine and theophylline can form six hydrogen bonds with the solvent compared to five for caffeine, suggesting that τ_2 should be approximately the same for paraxanthine and theophylline and slightly longer than for caffeine, but this is not observed.

An alternative explanation for the global τ_2 lifetime of the IVR intermediate states and the ring modes is that the ring and IVR intermediate states relax through common gateway modes.

Several theoretical calculations[79–81] and experiments[4,5,68,82–84] have suggested that intermolecular energy transfer can proceed through high-frequency solvent modes. Vibrational cooling (VC) dynamics of methylated xanthines and several other purine-derived nucleobases were studied earlier by Zhang, Chen, and Kohler in UV pump-IR probe experiments.[4] In the hot electronic ground state created following UIC, the asymmetric carbonyl stretch band near 1640 cm^{-1} in D_2O and 1665 cm^{-1} in CH_3CN (band 2 in the current study) is bleached and the bleach recovery of this band was monitored as a probe of VC dynamics. It was observed that the VC lifetimes in D_2O are correlated with the number of hydrogen bonds that each solute can donate to the solvent. Thus, the faster VC seen in D_2O by paraxanthine and theophylline, which can each donate a single hydrogen bond, was assigned to resonant energy transfer from the N-D bending mode of each to the D_2O bend mode at approximately 1200 cm^{-1} and N-D stretch resonant transfer to O-D stretch or to the O-D bend overtone. The latter pathway is absent in caffeine because it cannot donate a hydrogen bond to D_2O.

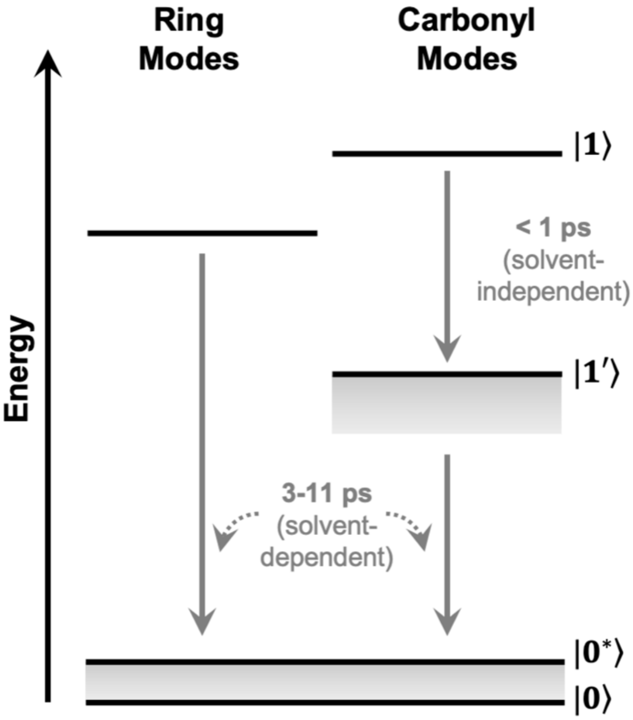

Figure 8. Kinetic scheme for vibrational relaxation of ring and carbonyl modes of the xanthine derivatives studied. The carbonyl modes undergo biphasic decay, with a nearly solvent-independent fast component

(IVR) which relaxes to a set of IVR intermediate states, $|1'\rangle$. The IVR intermediates thermalize on a slower, solvent-dependent timescale that matches the monoexponential decay of the ring modes in both solvents. In D_2O, the system remains in thermal equilibrium with a bath of solvent modes at elevated temperature created by absorption of the pump pulse.

We are now in a position to compare vibrational relaxation timescales obtained from IR-PP experiments (this study) with ones made by observing VC following UIC (ref. 4), a comparison that is seldom made in the literature. The time constants characterizing VC following UIC are identical to the time constants obtained in the current IR-PP studies in CH_3CN, and only slightly shorter in D_2O (**Table 4**). In D_2O, a similar, but less pronounced trend is observed. It is surprising that the lifetimes are similar considering that the experiments in Zhang et al. deposit over twenty times more excess vibrational energy than in the IR-PP experiment (38,000 cm^{-1} vs. 1,700 cm^{-1}). The nearly identical vibrational relaxation rates observed in both measurements are consistent with the proposal that VC proceeds via high-frequency modes of the solvent in D_2O and via lower-frequency in CH_3CN, which lacks the resonant pathway. Future studies addressing the nature of the IVR intermediate state and gateway modes to the solvent will clarify both the common relaxation of the ring and carbonyl modes observed in the present study. Such studies will also provide further insight into the role played by high-frequency solvent modes as key energy acceptors in vibrational cooling following electronic excitation following non-reactive (e.g., internal conversion) or chemical reaction dynamics (e.g., photoisomerization).

Table 4. Vibrational relaxation (VR)[a] vs. vibrational cooling (VC)[b] lifetimes (in ps).

	Caffeine		**Paraxanthine**		**Theophylline**	
	VR	**VC**	**VR**	**VC**	**VR**	**VC**
CH_3CN	10.1 ± 0.1	10 ± 3	10.3 ± 0.3	10 ± 3	10.8 ± 0.2	10 ± 3 ps
D_2O	5.5 ± 0.6	7.7 ± 0.9	4.3 ± 0.1	4 ± 1	3.3 ± 0.1	5.1 ± 0.8

[a] τ_2 from global fitting of each compound from Table 2.
[b] From Ref. 4.

IV. CONCLUSIONS

We have presented a detailed experimental and computational study of vibrational relaxation by several methylated xanthine derivatives in two polar solvents. The ring and carbonyl stretch modes differ in their vibrational relaxation dynamics even though they have similar fundamental frequencies. The carbonyl modes efficiently deposit the initial excitation in anharmonically coupled lower frequency solute modes via IVR. This initial sub-picosecond decay component is absent for the ring modes, likely because they are more weakly coupled to low-frequency solute modes. Despite these differences, both ring and carbonyl modes attain thermal equilibrium with the surrounding solvent molecules with the same solvent-dependent rates, implicating low-frequency solute modes as efficient sinks to the solvent via solvent-assisted IVR and/or IET. A nearly universal VC rate constant is obtained for VC studies with infrared or electronic excitation for a given purine derivative, despite more than an order of magnitude difference in excitation energy. This result suggests that experiments monitoring vibrational relaxation in the electronic ground state can be useful for understanding the relaxation of hot ground state molecules generated by UIC after photoexcitation.

The normal mode calculations reveal that methylation has a minimal effect on the vibrational mode character in the double-bond stretching region. However normal mode calculations are unable to account for the anharmonic interactions important in vibrational relaxation. Using IR-PP and 2D-IR spectroscopy, mode-specific couplings that dictate timescales for IVR are influenced by shifts in fundamental transition frequencies of the carbonyl modes, either by methylation or solvatochromism, despite the observation that methylation minimally perturbs vibrational normal mode character across the series of xanthine derivatives. This is supported by a two-fold increase in the time constant associated to IVR in theophylline in CH_3CN. Although methylation or simple chemical modifications are intended to simply tune hydrogen bonds to solvent molecules, these modifications can alter IVR pathways, even when linear IR spectra are nearly unchanged. The slow phase of relaxation is dictated by the solvent and is largely unaffected by these modifications. Future studies are required to address the specific role played by the solvent, which we expect to depend strongly upon the nature of the IVR-accepting states and whether these are efficient gateway modes to the solvent. Regardless, the current studies provide evidence for both mode-specific and statistical relaxation in nearly isoenergetic ring and carbonyl modes, which survives variation in both the number and placement of methyl substituents on the purine ring. It is concluded that caffeine, paraxanthine, and theophylline are promising candidates for future theoretical studies of VER in medium-sized molecules in protic and aprotic solvents.

V. EXPERIMENTAL AND COMPUTATIONAL METHODS

Caffeine (ReagentPlus®), paraxanthine (> 98%), and theophylline (anhydrous, ≥ 99%) were purchased from Sigma Aldrich (St. Louis, MO) and used as received. Solutions were prepared in acetonitrile (HPLC far UV grade, Acros Organics; Morris Plains, NJ) and heavy water (99.9 atom %D, Sigma Aldrich) in 10 mM, saturated (< 4 mM), and 7 mM concentrations for caffeine, paraxanthine, and theophylline, respectively. For all IR measurements, the sample was held between two CaF_2 windows separated by a 100 μm PTFE spacer to achieve a sample absorbance less than OD 0.3 in the 1500-1750 cm^{-1} spectral region. Samples were housed in a homemade demountable sample cell. Linear infrared absorption measurements were made using a JASCO FT/IR-4200 (Easton, MD). Room temperature spectra were recorded by averaging 50 spectra at 0.5 cm^{-1} resolution.

Degenerate infrared pump-probe and absorptive 2D-IR spectra were recorded using a PhaseTech 2DQuick IR spectrometer (PhaseTech Spectroscopy; Madison, WI) in the pump-probe geometry. The details of the laser setup have been described elsewhere.[85] The mid-IR pulse generated by the optical parametric amplifier was centered at 1640 cm^{-1} by DFG using a silver gallium sulfide, $AgGaS_2$, crystal. Approximately 7 μJ/pulse were directed into the germanium pulse shaper, with approximately 2.5 μJ/pulse (pump) incident on the sample. The spot sizes ($1/e^2$ beam radius) at the sample position were 350 μm and 200 μm for the pump and probe spot sizes, respectively, for all measurements. The 2D-IR spectra were collected using a partially rotating frame (1300 cm^{-1}) and 2-frame phase-cycling collected using a relative pump pulse pair phase of $\Delta\phi_{12} = 0$ and $\Delta\phi_{12} = \pi$ unless noted otherwise. Group velocity dispersion (GVD) and third-order dispersion (TOD) were mitigated by applying corrections to the pulse shaper masks.[32] The τ_1-axis was scanned from 0 to 4000 fs in 20 fs steps. Absorptive 2D-IR spectra were obtained at a waiting time, t_2 = 100 fs, unless stated otherwise. The 2D-IR spectra were collected under XXXX (parallel) and XXYY (perpendicular) polarization conditions over the double-bond stretching region (*ca*. 1500-1750 cm^{-1}). In a typical 2D-IR experiment, 3x10^6 laser shots (7500 2D-spectra, 2 frames, 201 delays) were collected to produce each 2D-IR spectrum for each polarization condition and t_2. Degenerate IR-PP signals were collected by fixing τ_1 = 0 ps and scanning the t_2 delay time from -10 ps to 60 ps using 233 nonlinearly spaced delay times. In a typical pump-probe measurement, each transient spectrum was recorded from 2000 laser shots (counting pump on and pump off) per delay time setting and 10 such spectra were averaged from separate scans to produce the final IR-PP spectrum for a given polarization condition (XXXX or XXYY).

Data processing and non-linear least squares fitting were performed using MATLAB® version 2022a (MathWorks).[86] Numerical Fourier transformation of the τ_1-axis was performed post-data collection. Prior to Fourier transformation, a Hamming window function was applied, and the data were zero-padded. The detection-frequency axis, $\omega_3/2\pi c$, was calibrated using water vapor lines. The pump-frequency axis, $\omega_1/2\pi c$, was calibrated using the pump-interference spectrum collected by scanning the delay time between shaper pulse pair from 0 to 4000 fs in 20 fs steps. The pump-interference spectrum was mapped onto the calibrated detection-frequency axis to determine the calibrated pump-frequency axis, $\omega_1/2\pi c$.

To better visualize the weaker features in the 2D-IR spectra, 21 equally spaced contours were drawn for signal amplitudes that fall in the interval $[0.1\,min, 0.1\,max]$, where min is the global signal minimum and max is the global signal maximum of the bisignate signals. These contours were drawn using a colormap in which red and blue colors show negative and positive signal amplitudes, respectively. An additional 9 contours were added from 10% to 100% of max in 10% steps on the positive side colored with the blue color used for the contour at $0.1\,max$. Finally, 9 further contours were added from 10% to 100% of *min* in 10% steps, colored with the red color of the $0.1\,min$ contour. This set of 39 total contours allows the intense as well as the weak signal features to be seen simultaneously. All IR-PP data were fit from $t_2 \geq 200$ fs to avoid coherent artifacts present at some of the detection frequencies. For more information on the data processing and global fitting procedures, see the Supplemental Material Section S3.

Quantum chemical calculations were performed using Gaussian 16.[87] Ground-state geometry optimizations were carried out with the B3LYP[88,89] density functional and the 6-311+G(d,p) basis set with the standard 5d spherical functions.[90–93] Harmonic vibrational frequency analyses were performed for each system at the same B3LYP/6-311+G(d,p)[88–91] level of theory; no scaling factors were employed for the extracted frequencies. Peak lineshapes were generated by convoluting stick spectra with an area normalized Gaussian, $f(\tilde{\nu}) = \sqrt{2\pi\sigma^2}\,\exp[-(\tilde{\nu}-\tilde{\nu}_k)^2/(2\sigma^2)]$, with FWHM = $2\sqrt{2\log 2}\,\sigma$. The starting geometries for the xanthine derivatives were obtained from published crystal structures.[94–96] Solvent effects on vibrational frequencies were accounted for by the addition of three (caffeine) and four (paraxanthine, theophylline) D_2O molecules near the hydrogen bond accepting and/or donating sites. For calculations in acetonitrile, a single explicit acetonitrile molecule was placed near the single hydrogen bond donating site of caffeine, paraxanthine, and theophylline. Finally, the calculations with explicit solvent molecules were conducted using the integral-equation formalism polarizable continuum model (IEF-PCM) for acetonitrile and water (H_2O was used since D_2O PCM is not available) to treat implicit solvent effects.[97–99] The optimized structures with explicit solvent molecules are shown in **Fig. S1-S3**. The inclusion of explicit water molecules was essential for obtaining good agreement between calculated and experiment values for the vibrational frequencies and angles between TDMs, mirroring conclusions by Peng et al.[45] from their study of hydrated nucleotides. Labile (i.e., all heteroatom-bound) hydrogen atoms were exchanged with deuterium atoms for simulations in D_2O. Further details of the electronic structure optimizations can be found in Section S1 of the Supplemental Material.

SUPPLEMENTARY MATERIAL

See supplementary material for additional data from normal mode calculations (atomic displacement vectors, IR intensities, atomic coordinates of equilibrium geometry structures), fitting of the on- and off-diagonal anharmonic shifts, additional infrared pump-probe spectra (early-time evolution of the IR-PP spectra, temperature-difference spectra of hot D_2O), the global fitting procedure (amplitudes of biphasic decays, best and worst global fit), the model of incoherent population transfer and waiting-time-dependent 2D-IR spectra of caffeine, a derivation of the polarization-dependent IR-PP spectra with calculated polarization-dependent IR-PP signals, and the tier model for IVR.

ACKNOWLEDGMENTS

Work at The Ohio State University was supported by a grant from the US National Science Foundation (CHE-1800471). ATH thanks Dr. Yuyuan Zhang for helpful discussions regarding time-resolved infrared spectroscopy. Computational resources from the Ohio Supercomputer Center are gratefully acknowledged.

AUTHOR DECLARATIONS

Conflict of Interest

The authors have no conflicts to disclose.

Author Contributions

Alex T. Hanes: Conceptualization (equal); Formal Analysis (lead); Investigation (equal); Visualization (lead); Writing – original draft (lead); Writing – review & editing (equal). **Christopher Grieco**: Conceptualization (equal); Formal Analysis (equal); Investigation (equal); Writing – review & editing (equal). **Remy F. Lalisse**: Formal Analysis (supporting); Investigation (equal); Writing – review & editing (equal); Visualization (supporting). **Christopher M. Hadad**: Formal Analysis (supporting); Investigation (equal); Supervision (equal); Writing – review & editing (equal). **Bern Kohler**: Conceptualization (equal); Funding acquisition (lead); Supervision (equal); Writing – original draft (supporting); Writing – review & editing (equal).

DATA AVAILABILITY

The data that support the findings of this study are available from the corresponding author upon reasonable request.

REFERENCES

[1] M. Barbatti, A.J.A. Aquino, J.J. Szymczak, D. Nachtigallová, P. Hobza, and H. Lischka, Proc. Natl. Acad. Sci. U. S. A. **107**, 21453 (2010).

[2] D.B. Bucher, B.M. Pilles, T. Carell, and W. Zinth, Proc. Natl. Acad. Sci. **111**, 4369 (2014).

[3] L. Martinez-Fernandez and R. Improta, Faraday Discuss. **207**, 199 (2018).

[4] Y. Zhang, J. Chen, and B. Kohler, J. Phys. Chem. A **117**, 6771 (2013).

[5] C.T. Middleton, B. Cohen, and B. Kohler, J. Phys. Chem. A **111**, 10460 (2007).

[6] J.-M.L. Pecourt, J. Peon, and B. Kohler, J. Am. Chem. Soc. **123**, 10370 (2001).

[7] J. Chen and B. Kohler, Phys. Chem. Chem. Phys. **14**, 10677 (2012).

[8] C.E. Crespo-Hernandez and B. Kohler, J. Phys. Chem. B **108**, 11182 (2004).

[9] C.E. Crespo-Hernandez, B. Cohen, and B. Kohler, Nature **436**, 1141 (2005).

[10] B. Kohler, J. Phys. Chem. Lett. **1**, 2047 (2010).

[11] J.C. Owrutsky, D. Raftery, and R.M. Hochstrasser, Annu Rev Phys Chem **45**, 519 (1994).

[12] P. Hamm, S.M. Ohline, and W. Zinth, J. Chem. Phys. **106**, 519 (1997).

[13] T. Uzer and W.H. Miller, Phys. Rep. **199**, 73 (1991).

[14] S.A. Kovalenko, R. Schanz, V.M. Farztdinov, H. Hennig, and N.P. Ernsting, Chem. Phys. Lett. **323**, 312 (2000).

[15] Y. Kimura, M. Fukuda, O. Kajimoto, and M. Terazima, J. Chem. Phys. **125**, 194516 (2006).

[16] T. Kiba, S. Sato, S. Akimoto, T. Kasajima, and I. Yamazaki, J. Photochem. Photobiol. Chem. **178**, 201 (2006).

[17] S.A. Kovalenko, R. Schanz, H. Hennig, and N.P. Ernsting, J. Chem. Phys. **115**, 3256 (2001).

[18] A. Pigliucci, G. Duvanel, L.M.L. Daku, and E. Vauthey, J. Phys. Chem. A **111**, 6135 (2007).

[19] K. Ohta and K. Tominaga, Chem. Phys. **341**, 310 (2007).

[20] H.D. Pandey and D.M. Leitner, J. Phys. Chem. A **122**, 6856 (2018).

[21] A.J. Schmitz, H.D. Pandey, F. Chalyavi, T. Shi, E.E. Fenlon, S.H. Brewer, D.M. Leitner, and M.J. Tucker, J. Phys. Chem. A **123**, 10571 (2019).

[22] M.F. DeCamp, L. DeFlores, J.M. McCracken, A. Tokmakoff, K. Kwac, and M. Cho, J. Phys. Chem. B **109**, 11016 (2005).

[23] H. Bian, J. Li, X. Wen, and J. Zheng, J. Chem. Phys. **132**, 184505 (2010).

[24] H. Bian, X. Wen, J. Li, and J. Zheng, J. Chem. Phys. **133**, 034505 (2010).

[25] H. Bian, X. Wen, J. Li, H. Chen, S. Han, X. Sun, J. Song, W. Zhuang, and J. Zheng, Proc. Natl. Acad. Sci. **108**, 4737 (2011).

[26] H. Bian, W. Zhao, and J. Zheng, J. Chem. Phys. **131**, 124501 (2009).

[27] B.A. West, J.M. Womick, and A.M. Moran, J. Chem. Phys. **135**, 114505 (2011).

[28] M. Cho, *Two-Dimensional Optical Spectroscopy* (CRC Press, Boca Raton, 2009).

[29] P. Hamm and M.T. Zanni, *Concepts and Methods of 2D Infrared Spectroscopy* (Cambridge University Press, Cambridge ; New York, 2011).

[30] S.K. Srivastava and V.B. Singh, Spectrochim. Acta. A. Mol. Biomol. Spectrosc. **115**, 45 (2013).

[31] R. Fernández-Terán, J. Ruf, and P. Hamm, Inorg. Chem. **59**, 7721 (2020).

[32] P. Hamm and M. Zanni, Camb. Core (2011).

[33] M. Khalil, N. Demirdöven, and A. Tokmakoff, J. Phys. Chem. A **107**, 5258 (2003).

[34] A. Tokmakoff, J. Chem. Phys. **105**, 1 (1996).

[35] H.-S. Tan, I.R. Piletic, and M.D. Fayer, JOSA B **22**, 2009 (2005).

[36] B. Auer, R. Kumar, J.R. Schmidt, and J.L. Skinner, Proc. Natl. Acad. Sci. **104**, 14215 (2007).

[37] H.J. Bakker, Y.L.A. Rezus, and R.L.A. Timmer, J. Phys. Chem. A **112**, 11523 (2008).

[38] S.Yu. Venyaminov and F.G. Prendergast, Anal. Biochem. **248**, 234 (1997).

[39] W.J. Schreier, T.E. Schrader, F.O. Koller, P. Gilch, C.E. Crespo-Hernández, V.N. Swaminathan, T. Carell, W. Zinth, and B. Kohler, Science **315**, 625 (2007).

[40] P. Kletting, T. Kull, S.N. Reske, and G. Glatting, Phys. Med. Biol. **54**, N501 (2009).

[41] P. Hamm and M. Zanni, *Concepts and Methods of 2D Infrared Spectroscopy* (Cambridge University Press, Cambridge, 2011).

[42] P.B. Balbuena, W. Blocker, R.M. Dudek, F.A. Cabrales-Navarro, and P. Hirunsit, J. Phys. Chem. A **112**, 10210 (2008).

[43] R.A. Nyquist and S.L. Fiedler, Vib. Spectrosc. **8**, 365 (1995).

[44] E.T.J. Nibbering and T. Elsaesser, Chem. Rev. **104**, 1887 (2004).

[45] C.S. Peng, K.C. Jones, and A. Tokmakoff, J. Am. Chem. Soc. **133**, 15650 (2011).

[46] G. Wang, F. Li, J. Zhao, Y. Wu, and J. Wang, ChemistrySelect **3**, 4374 (2018).

[47] L.P. DeFlores, Z. Ganim, S.F. Ackley, H.S. Chung, and A. Tokmakoff, J. Phys. Chem. B **110**, 18973 (2006).

[48] K. Blum, *Density Matrix Theory and Applications* (Springer US : Imprint: Springer, Boston, MA, 1981).

[49] V. May and O. Kühn, *Charge and Energy Transfer Dynamics in Molecular Systems*, 3rd edition (Wiley-VCH, Weinheim, 2011).

[50] V. Cervetto, J. Helbing, J. Bredenbeck, and P. Hamm, J. Chem. Phys. **121**, 5935 (2004).

[51] S. Park and M. Ji, ChemPhysChem **12**, 799 (2011).

[52] P. Hamm, M. Lim, W.F. DeGrado, and R.M. Hochstrasser, J. Chem. Phys. **112**, 1907 (2000).

[53] O. Golonzka, M. Khalil, N. Demirdöven, and A. Tokmakoff, J. Chem. Phys. **115**, 10814 (2001).

[54] X. He, P. Yu, J. Zhao, and J. Wang, J. Phys. Chem. B **121**, 9411 (2017).

[55] C.G. Elles and F.F. Crim, Annu. Rev. Phys. Chem. **57**, 273 (2006).

[56] A. Nitzan, *Chemical Dynamics in Condensed Phases* (Oxford University Press, 2006).

[57] D.M. Jonas, Annu. Rev. Phys. Chem. **54**, 425 (2003).

[58] S.H. Schneider, H.T. Kratochvil, M.T. Zanni, and S.G. Boxer, J. Phys. Chem. B **121**, 2331 (2017).

[59] S.T. Roberts, J.J. Loparo, and A. Tokmakoff, J. Chem. Phys. **125**, 084502 (2006).

[60] J.T. King, J.M. Anna, and K.J. Kubarych, Phys. Chem. Chem. Phys. **13**, 5579 (2011).

[61] J.A. Myers, K.L.M. Lewis, P.F. Tekavec, and J.P. Ogilvie, Opt. Express **16**, 17420 (2008).

[62] G. Herzberg, *Molecular Spectra and Molecular Structure: Volume II: Infrared and Raman Spectra of Polyatomic Molecules: Infrared and Raman Spectra of Polyatomic Molecules* (n.d.).

[63] M. Khalil, N. Demirdöven, and A. Tokmakoff, J. Chem. Phys. **121**, 362 (2004).

[64] K. Wynne and R.M. Hochstrasser, Chem. Phys. **171**, 179 (1993).

[65] C. Galli, K. Wynne, S.M. LeCours, M.J. Therien, and R.M. Hochstrasser, Chem. Phys. Lett. **206**, 493 (1993).

[66] R.S. Knox and D. Gülen, Photochem. Photobiol. **57**, 40 (1993).

[67] D.J. Shaw, K. Adamczyk, P.W.J.M. Frederix, N. Simpson, K. Robb, G.M. Greetham, M. Towrie, A.W. Parker, P.A. Hoskisson, and N.T. Hunt, J. Chem. Phys. **142**, 212401 (2015).

[68] C.G. Elles, M.J. Cox, and F.F. Crim, J. Chem. Phys. **120**, 6973 (2004).

[69] A. Maitra, S. Sarkar, D.M. Leitner, and J.M. Dawlaty, J. Phys. Chem. Lett. **12**, 7818 (2021).

[70] G. Hithell, P.M. Donaldson, G.M. Greetham, M. Towrie, A.W. Parker, G.A. Burley, and N.T. Hunt, Chem. Phys. **512**, 154 (2018).

[71] P. Hamm, M. Lim, and R.M. Hochstrasser, J. Phys. Chem. B **102**, 6123 (1998).

[72] B.H. Jones, C.J. Huber, and A.M. Massari, J. Phys. Chem. A **117**, 6150 (2013).

[73] M. Lim and R.M. Hochstrasser, J. Chem. Phys. **115**, 7629 (2001).

[74] L. Piatkowski and H.J. Bakker, J. Chem. Phys. **136**, 164504 (2012).

[75] L. Piatkowski and H.J. Bakker, J. Phys. Chem. A **114**, 11462 (2010).

[76] T.J. Minehardt and R.E. Wyatt, Chem. Phys. Lett. **312**, 485 (1999).

[77] K.F. Freed and A. Nitzan, J. Chem. Phys. **73**, 4765 (1980).

[78] M. Banno, K. Ohta, and K. Tominaga, J. Phys. Chem. A **112**, 4170 (2008).

[79] C.P. Lawrence and J.L. Skinner, J. Chem. Phys. **119**, 1623 (2003).

[80] Y. Zhang, H. Fujisaki, and J.E. Straub, J. Chem. Phys. **130**, 025102 (2009).

[81] Y. Zhang, H. Fujisaki, and J.E. Straub, J. Phys. Chem. A **113**, 3051 (2009).

[82] T. Siebert, B. Guchhait, Y. Liu, R. Costard, and T. Elsaesser, J. Phys. Chem. B **119**, 9670 (2015).

[83] J. Assmann, A. Charvat, D. Schwarzer, C. Kappel, K. Luther, and B. Abel, J. Phys. Chem. A **106**, 5197 (2002).

[84] J. Assmann, R. von Benten, A. Charvat, and B. Abel, J. Phys. Chem. A **107**, 5291 (2003).

[85] C. Grieco, A.T. Hanes, L. Blancafort, and B. Kohler, J. Phys. Chem. A **123**, 5356 (2019).

[86] MATLAB, *Version 9.12.0 (R2022a)*, Natick, Massachusetts (The MathWorks Inc., 2022).

[87] M.J. Frisch, G.W. Trucks, H.B. Schlegel, G.E. Scuseria, M.A. Robb, J.R. Cheeseman, G. Scalmani, V. Barone, G.A. Petersson, H. Nakatsuji, X. Li, M. Caricato, A.V. Marenich, J. Bloino, B.G. Janesko, R. Gomperts, B. Mennucci, H.P. Hratchian, J.V. Ortiz, A.F. Izmaylov, J.L. Sonnenberg, Williams, F. Ding, F. Lipparini, F. Egidi, J. Goings, B. Peng, A. Petrone, T. Henderson, D. Ranasinghe, V.G. Zakrzewski, J. Gao, N. Rega, G. Zheng, W. Liang, M. Hada, M. Ehara, K. Toyota, R. Fukuda, J. Hasegawa, M. Ishida, T. Nakajima, Y. Honda, O. Kitao, H. Nakai, T. Vreven, K. Throssell, J.A. Montgomery Jr., J.E. Peralta, F. Ogliaro, M.J. Bearpark, J.J. Heyd, E.N. Brothers, K.N. Kudin, V.N. Staroverov, T.A. Keith, R. Kobayashi, J. Normand, K. Raghavachari, A.P. Rendell, J.C. Burant, S.S. Iyengar, J. Tomasi, M. Cossi, J.M. Millam, M. Klene, C. Adamo, R. Cammi, J.W. Ochterski, R.L. Martin, K. Morokuma, O. Farkas, J.B. Foresman, and D.J. Fox, (2016).

[88] A.D. Becke, J. Chem. Phys. **98**, 5648 (1993).

[89] M.M.N. Wolf, C. Schumann, R. Gross, T. Domratcheva, and R. Diller, J. Phys. Chem. B **112**, 13424 (2008).

[90] A.D. McLean and G.S. Chandler, J. Chem. Phys. **72**, 5639 (1980).

[91] R. Krishnan, J.S. Binkley, R. Seeger, and J.A. Pople, J. Chem. Phys. **72**, 650 (1980).

[92] B. Roos, A. Veillard, and G. Vinot, Theor. Chim. Acta **20**, 1 (1971).

[93] K. Raghavachari and G.W. Trucks, J. Chem. Phys. **91**, 1062 (1989).

[94] Y. Ebisuzaki, P.D. Boyle, and J.A. Smith, Acta Crystallogr. C **53**, 777 (1997).

[95] L. Carlucci and A. Gavezzotti, Chem. Weinh. Bergstr. Ger. **11**, 271 (2004).

[96] C.W. Lehmann and F. Stowasser, Chem. Weinh. Bergstr. Ger. **13**, 2908 (2007).

[97] S. Miertuš, E. Scrocco, and J. Tomasi, Chem. Phys. **55**, 117 (1981).

[98] S. Miertus̃ and J. Tomasi, Chem. Phys. **65**, 239 (1982).

[99] J.L. Pascual-ahuir, E. Silla, and I. Tuñon, J. Comput. Chem. **15**, 1127 (1994).

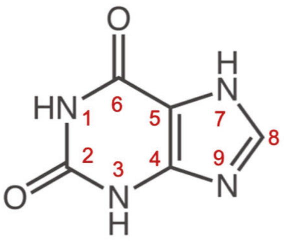

Xanthine

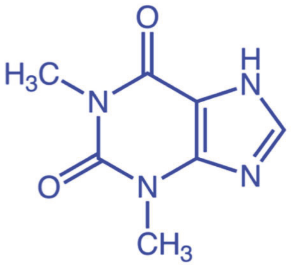

Theophylline (T)
(1,3-dimethylxanthine)

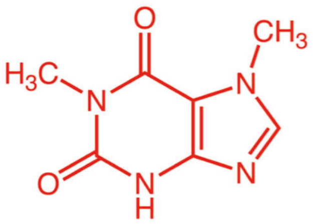

Paraxanthine (P)
(1,7-dimethylxanthine)

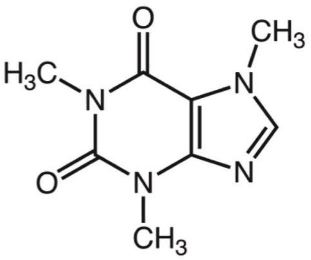

Caffeine (C)
(1,3,7-trimethylxanthine)

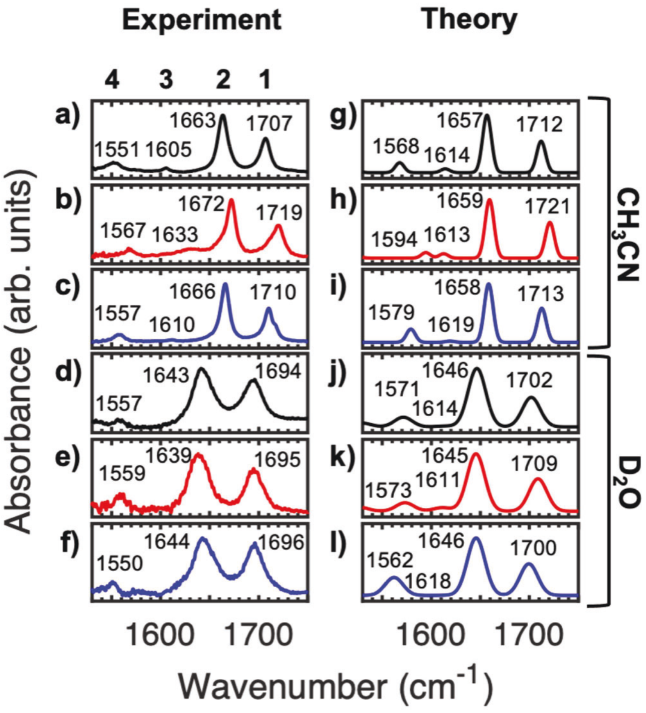
Experiment
Theory
4
3
2
1
a)
1663
1707
1551
1605
b)
1672
1719
1567
1633
c)
1666
1710
1557
1610
d)
1643
1694
1557
e)
1639
1695
1559
f)
1644
1696
1550
g)
1657
1712
1568
1614
h)
1659
1721
1594
1613
i)
1658
1713
1579
1619
j)
1646
1702
1571
1614
k)
1645
1709
1611
1573
l)
1646
1700
1562
1618
CH_3CN
D_2O
Absorbance (arb. units)
1600
1700
1600
1700
Wavenumber (cm^{-1})

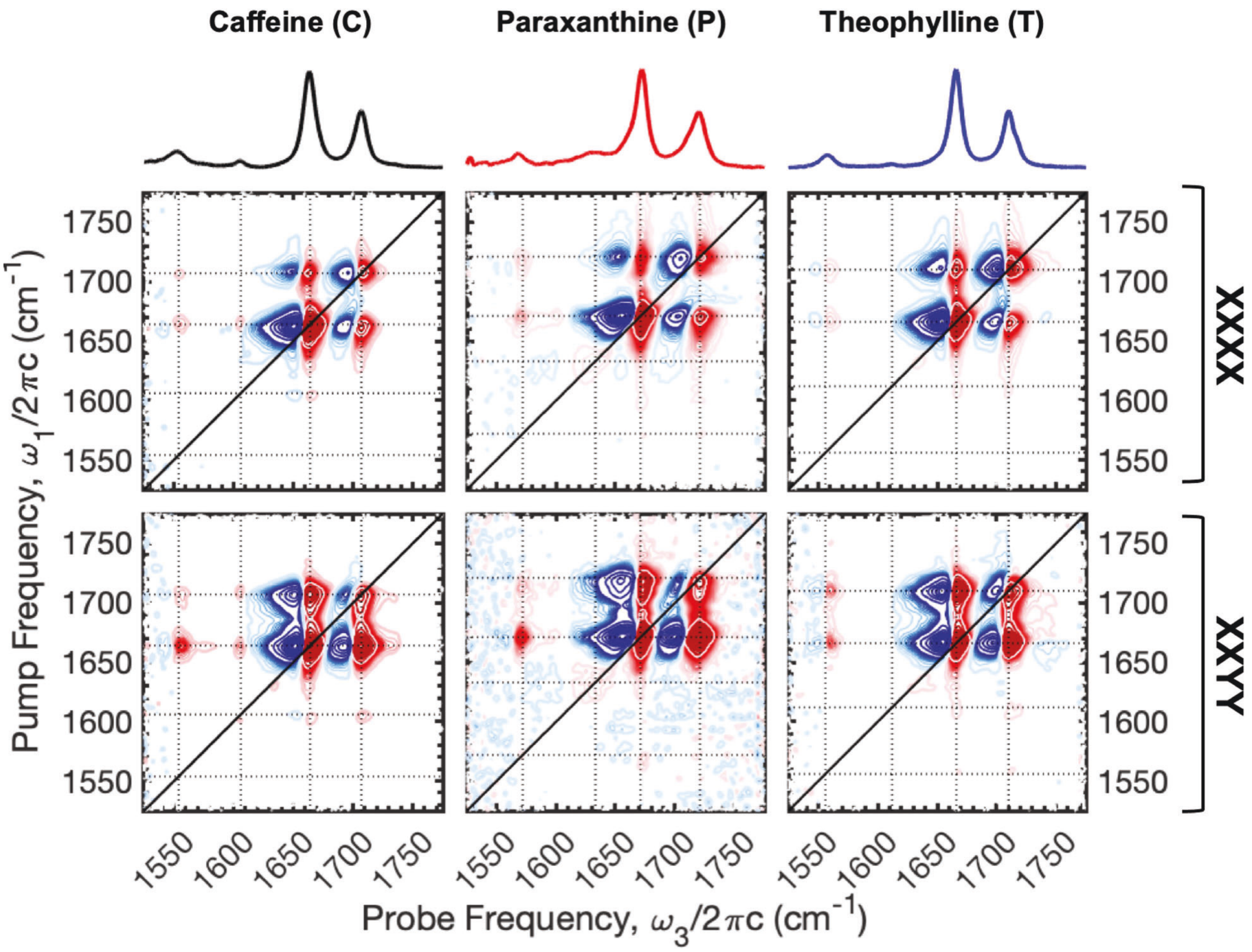
Caffeine (C)
Paraxanthine (P)
Theophylline (T)
XXXX
XXYY
1750
1700
1650
1600
1550
Pump Frequency, $\omega_1/2\pi c$ (cm^{-1})
Probe Frequency, $\omega_3/2\pi c$ (cm^{-1})

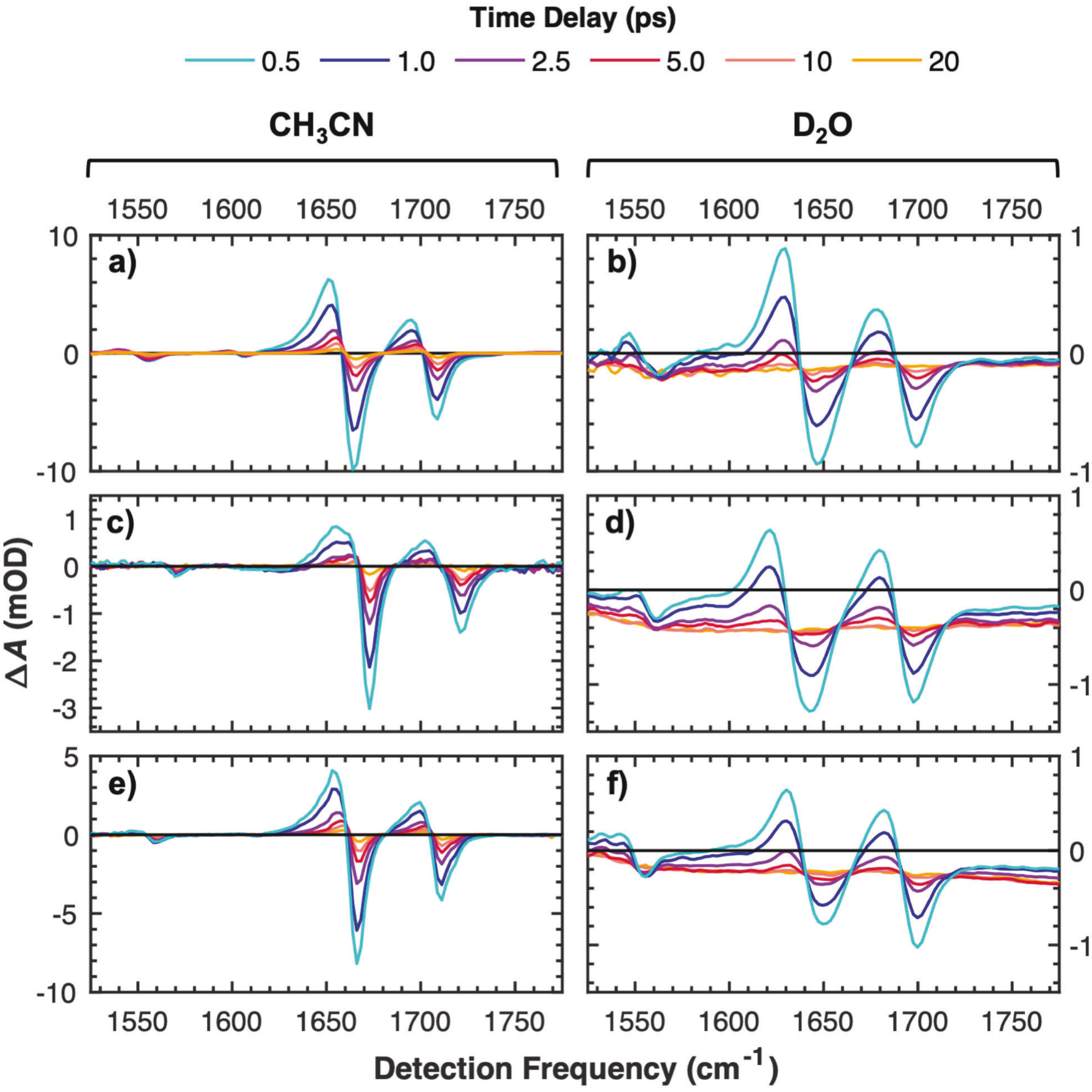
Time Delay (ps)
0.5
1.0
2.5
5.0
10
20
CH$_3$CN
D$_2$O
a)
b)
c)
d)
e)
f)
ΔA (mOD)
Detection Frequency (cm^{-1})
1550
1600
1650
1700
1750
10
0
-10
1
0
-1
-2
-3
5
-5
1
0
-1

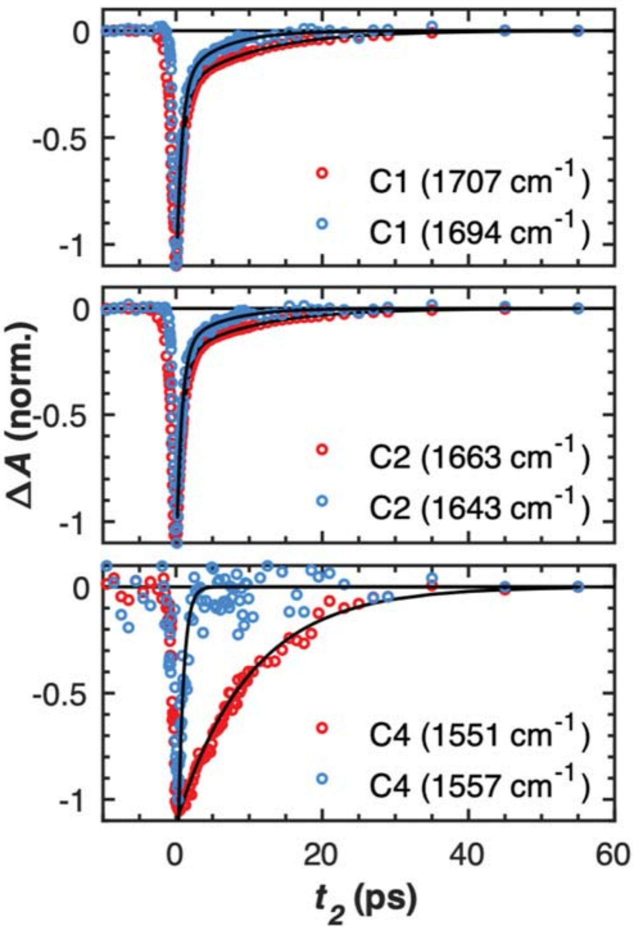
0
-0.5
-1
C1 (1707 cm^{-1})
C1 (1694 cm^{-1})
C2 (1663 cm^{-1})
C2 (1643 cm^{-1})
C4 (1551 cm^{-1})
C4 (1557 cm^{-1})
ΔA (norm.)
0
20
40
60
t2 (ps)

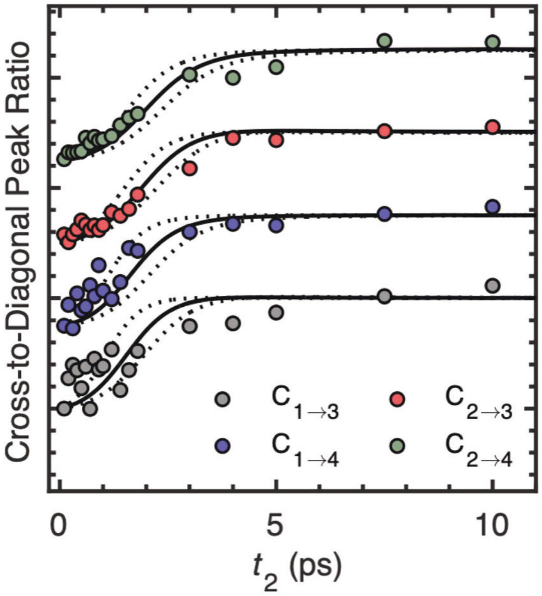
Cross-to-Diagonal Peak Ratio
t_2 (ps)
0
5
10
$C_{1\to3}$
$C_{1\to4}$
$C_{2\to3}$
$C_{2\to4}$

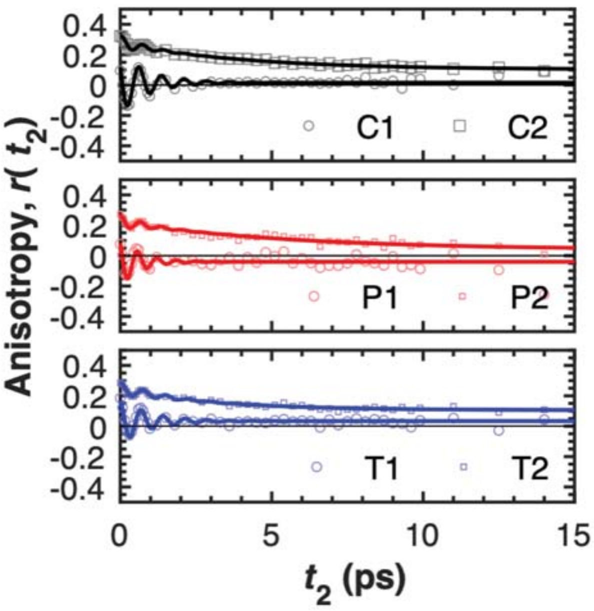
Anisotropy, $r(t_2)$
0.4
0.2
0
-0.2
-0.4
C1
C2
P1
P2
T1
T2
0
5
10
15
t_2 (ps)

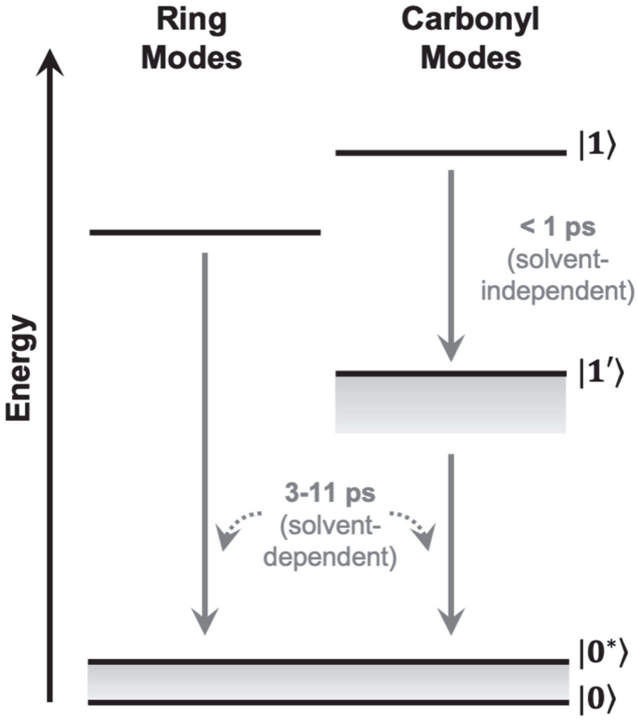

Ring Modes
Carbonyl Modes
Energy
|1⟩
< 1 ps (solvent-independent)
|1′⟩
3-11 ps (solvent-dependent)
|0*⟩
|0⟩